J. Fluid Mech. (2024), *vol*. 980, A50, doi:10.1017/jfm.2024.37

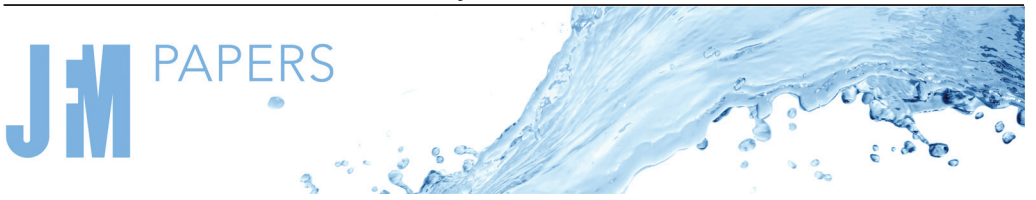

Effects of streamwise rotation on helicity and vortex in channel turbulence

Running Hu[1,2], **Xinliang Li**[1,2] **and Changping Yu**[1,†]

[1]LHD, Institute of Mechanics, Chinese Academy of Sciences, Beijing 100190, PR China

[2]School of Engineering Science, University of Chinese Academy of Sciences, Beijing 100049, PR China

(Received 3 May 2023; revised 26 October 2023; accepted 4 January 2024)

Helicity plays a key role in the evolution of vortex structures and turbulent dynamics. The helicity dynamics and vortex structures in streamwise-rotating channel turbulence are discussed in this paper using the helicity budget equation and the differentiated second-order structure function equation of helicity. Generally, rotation and Reynolds numbers exhibit opposing effects on the interscale helicity dynamics and the vortices. Under the buffer layer, the positions of the helicity peaks are proportional to the ratio between the Reynolds and rotation numbers. The mechanism is related to the opposing effects of convection and rotation. Rotation directly affects the helicity balance through the Coriolis term and corresponding pressure term. In the buffer layer, the scale helicity is negative at small scales but positive at large scales, which is mainly induced by the spatial effects (the production and the spatial turbulent convection) but reduced by interscale cascades. Examination of structures reveals the close association between scale helicity and streaks, with streak lift angles exhibiting an increase with rotation and a decrease with Reynolds numbers. In the log-law layer, the Coriolis terms and corresponding pressure terms are proportional to the rotation numbers but remain independent of the Reynolds numbers. The negative scale helicity is forward cascaded towards small scales. Generally, spanwise vortices in the log-law layer are related to sweep events and forward cascades. Our findings indicate that these spanwise vortices are suppressed by rotation but recover with increasing Reynolds numbers, aligning with the effects observed in the scale helicity balance.

Key words: rotating turbulence, channel flow, turbulence simulation

1. Introduction

Rotation is a critical component in turbomachinery as it is responsible for transferring energy between the rotor and the fluid medium (Weiss *et al.* 2019; Jing & Ducoin 2020;

† Email address for correspondence: cpyu@imech.ac.cn

Liu *et al.* 2020). Channel turbulence with rotation is a simplified model for turbulence observed in rotating machinery. As rotation is introduced, the wall-bound turbulence is strongly modified. Based on the Lie group method, Oberlack (2001) proposed the linear profile of the mean velocity in the spanwise-rotation channel turbulence. Specifically, in the channel centre, the streamwise mean velocity is linear and the slope is proportional to the rotation rates (Johnston, Halleent & Lezius 1972). With increasing rotation rates, the 'second plateau' emerges in the Reynolds shear stress, resulting in a parabolic streamwise mean velocity profile (Xia, Shi & Chen 2016). In addition, large longitudinal Taylor–Görtler-like (TG) vortices appear in the cross-section (Kristoffersen & Andersson 1993; Dai, Huang & Xu 2016). In streamwise-rotating channel turbulence, Oberlack *et al.* (2006) used the group analysis and large eddy simulation (LES) to identify the secondary mean flow, i.e. the spanwise mean velocity perpendicular to the main flow. Furthermore, the secondary mean flow is reversed around the channel centre, which has been verified through the stability analysis (Masuda, Fukuda & Nagata 2008) and various direct numerical simulation (DNS) (Yang, Su & Wu 2010; Yang & Wang 2018; Yang *et al.* 2018; Dai, Huang & Xu 2019; Yan, Li & Yu 2022). Yang *et al.* (2010) expanded the helical wave decomposition (HWD) (Waleffe 1992, 1993) to the periodic channel domain and found that the inertial wave is responsible for the secondary mean flow in the streamwise-rotating channel turbulence. Yang & Wang (2018) found that the necessary computational configuration is sensitive to the rotation rates and gave the three criteria for fine configurations. In terms of flow structures, Dai *et al.* (2019) found the inclined streamwise vortices in streamwise-rotating channel turbulence, where the inclination angles are inversely proportional to the rotation rates. Furthermore, Yang & Wang (2018) found that when the rotation number $Ro_\tau = 150$, the inclined angle is negligible and TG vortices appear.

In terms of interscale transfers, the second-order structure function was introduced by Kolmogorov (1941). The budget equation of the second-order structure function is named as the Kolmogorov equation. Then, the generalized Kolmogorov equation (GKE) was used in the transfers of wall-bound flows (Danaila *et al.* 2001; Marati, Casciola & Piva 2004), including the channel turbulence (Marati *et al.* 2004; Cimarelli, De Angelis & Casciola 2013; Cimarelli *et al.* 2015, 2016) and separated flows (Mollicone *et al.* 2018). Compared with the spectral analysis, the second-order structure function provides a natural definition of scales in inhomogeneous turbulence and the GKE methods could describe the interscale dynamics in inhomogeneous turbulence. For example, Cimarelli *et al.* (2016) investigated the interscale transfers in the wall-normal directions and found two ways of interscale energy transfers, consistent with the classical attached vortex model (Marusic & Monty 2019). Recently, Gatti *et al.* (2020) used the generalized Kolmogorov equation for the Reynolds stresses to study the roles of Reynolds stresses in interscale dynamics, where three examples were discussed in detail. In the streamwise-rotating channel turbulence, Yang *et al.* (2020*b*) used spectral analysis to study the interscale transfers and found four key processes for sustaining the motion of large-scale TG vortices. Hu, Li & Yu (2023) analysed the multiscale behaviours of the inclined vortices and explained the mechanisms through the generalized Kolmogorov equation for Reynolds stresses. Yang *et al.* (2018) decomposed the pressure fluctuating field into the two parts induced by rotation and convection and they identified the effects of rotation on the pressure fields through spectral analysis.

Helicity is the contraction of the velocity and vorticity, and is another second-order inviscid invariant in addition to energy in three-dimensional turbulence (Moffatt & Tsinober 1992; Alexakis & Biferale 2018). The conservation of helicity stems from the conservation of vorticity line topology and Helmholtz's laws (Davidson 2016).

Therefore, helicity intrinsically represents the topology of the vortices. Specifically, there are three typical helical structures: linkage, twisting and writhing (Irvine 2018). Helicity plays a vital role in mixing, instability (Tsinober 2019) and dynamos in magnetohydrodynamic turbulence (Pouquet & Yokoi 2022). Traditionally, the study of helicity mainly concentrated on the homogeneous turbulence, such as the scaling laws (Brissaud *et al.* 1973; Teimurazov *et al.* 2018), decaying laws (Polifke & Shtilman 1989; Biferale *et al.* 2003), HWD (Waleffe 1992), intermittency (Chen *et al.* 2003*b*) and cascades (Alexakis & Biferale 2018; Chen, Chen & Eyink 2003*a*). In anisotropic turbulent flows, there is also valuable research. Pelz *et al.* (1985) found that in channel turbulence, in the inner layer with high dissipation, the normalized helicity is evenly probable, but the normalized helicity tends to be greatly distinguished. Hiejima (2020) studied the instability of Batchelor vortices and found the helicity instability, which is related to a negative helicity with a large swirl number. Povitsky (2017) studied the three-dimensional flow with elevated helicity in the driven cavity and confirmed that the cases with strong helicity mix better than several other cases. In the presence of the boundary layer, streamwise-rotating channel turbulence is a natural helical flow. The coupling effects between helicity and the boundary layer have not been taken into consideration until recent years. Yang & Wang (2018) introduced the HWD in this flow and investigated the transfer process in the whole domain. Yu *et al.* (2022) studied the helicity distribution in such a flow and performed simple multiscale analysis related to the dual channel of the helicity cascades. The dual channel process was first found in homogeneous turbulence (Yan *et al.* 2022) and then generalized to the streamwise-rotating channel turbulence by Yu *et al.* (2022). Nevertheless, in streamwise-rotating channel turbulence, the interscale helicity dynamics and their relations with vortices have not been thoroughly studied.

In this paper, we discuss the effects of rotation and Reynolds numbers on the helicity dynamics through the helicity budgets, the differentiated structure function equation as well as the vortex structures. The paper is organized as follows. In § 2, we give the details of simulations and basic statistics. Next, in § 3, we first derive the budget equation for the scale helicity and then analyse related dynamics. Then, the relation between helicity and the vortices is discussed in § 4. Finally, conclusions are given in § 5.

2. Numerical simulations

The governing equations, i.e. the incompressible Navier–Stokes (N–S) equations, can be written as

$$\left.\begin{aligned} &\frac{\partial U_i}{\partial t} + U_j\frac{\partial U_i}{\partial x_j} = -\frac{1}{\rho}\frac{\partial P}{\partial x_i} + \nu\frac{\partial^2 U_i}{\partial x_i x_i} + 2\epsilon_{ij1}U_j\Omega - \frac{\Pi}{\rho}\delta_{i1}, \\ &\frac{\partial U_i}{\partial x_i} = 0, \end{aligned}\right\} \tag{2.1}$$

where U_i is the velocity, P is the total pressure including the centrifugal effects (Davidson 2013), ρ is the density, ν is the kinematic viscosity, Ω is the rotation rate, Π is a constant pressure gradients and δ_{ij} is the Kronecker delta. The computational configurations are shown in table 1. The Reynolds number $Re_\tau = u_\tau h/\nu$ ranges from 180 to 590 and the rotation number $Ro_\tau = 2\Omega h/u_\tau$ ranges from 0 to 60, where u_τ is the friction velocity and $h = 1$ is the channel half-width. The cases used in this paper have reached the statistical equilibrium states. For the averaged quantities, the results in this paper are averaged over 40 h/u_τ after the statistical steady state is reached. In addition, the friction velocity u_τ and

Case	$L_1 \times 2h \times L_3$	$N_1 \times N_y \times N_3$	Re_τ	Ro_τ
ST00	$32\pi \times 2 \times 8\pi$	$1024 \times 128 \times 512$	180	0
ST07	$32\pi \times 2 \times 8\pi$	$1024 \times 128 \times 512$	180	7.5
ST07R	$32\pi \times 2 \times 8\pi$	$2048 \times 192 \times 1024$	395	7.5
ST07RR	$32\pi \times 2 \times 8\pi$	$4096 \times 256 \times 2048$	590	7.5
ST15	$64\pi \times 2 \times 8\pi$	$2048 \times 128 \times 512$	180	15
ST15R	$64\pi \times 2 \times 8\pi$	$4096 \times 192 \times 1024$	395	15
ST30	$128\pi \times 2 \times 8\pi$	$4096 \times 128 \times 512$	180	30
ST60S	$128\pi \times 2 \times 8\pi$	$4096 \times 128 \times 512$	180	60

Table 1. Computational descriptions of simulations.

the viscous length scale $\delta = \nu/u_\tau$ are used to normalize the quantities in the following analyses, which are marked by the superscript '+'. Additionally, the error bars of the main results are evaluated using the standard deviation and are indicated in the figure captions and Appendix A.2.

2.1. *Helicity*

The mean helicity H, fluctuating helicity $\langle h \rangle$ and their components (H_i and $\langle h_i \rangle$) are defined as

$$H = \sum_{i=1}^{3} H_i = \sum_{i=1}^{3} \left\langle U_{\underline{i}} \right\rangle \left\langle W_{\underline{i}} \right\rangle, \quad \langle h \rangle = \sum_{i=1}^{3} \langle h_i \rangle = \sum_{i=1}^{3} \left\langle u_{\underline{i}} \omega_{\underline{i}} \right\rangle, \tag{2.2a,b}$$

where $W_i = \epsilon_{ijk} \partial U_k / \partial x_j$ is the vorticity, u_i is the fluctuating velocity, $\omega_i = \epsilon_{ijk} \partial u_k / \partial x_j$ is the fluctuating vorticity, the underlines in the subscript represent no contraction, and $\langle \cdot \rangle$ represents the average on the x_1 and x_3 direction. The mean velocities and vorticities are given in Appendix A.1 for reference.

Figure 1(*a*,*b*) shows the mean helicity H and its decomposition H_i, respectively. As shown in figure 1(*a*), the mean helicity is positive around the wall but negative around the channel centre. However, with increasing rotation, the mean helicity is extended to the vicinity of the wall. In contrast, as Re_τ increases, the mean helicity is reduced. The decomposition in figure 1(*b*) does not include the wall-normal component, because $H_2 = \langle U_2 \rangle \langle W_2 \rangle = 0$. In addition, when $x_2^+ \lessapprox 4$, $H_1 \approx -H_3$, which is because

$$\left.\begin{aligned} \langle U_1 \rangle \langle W_1 \rangle = \langle U_1 \rangle \left\langle \frac{\partial U_3}{\partial x_2} \right\rangle \approx \left\langle \frac{\partial U_1}{\partial x_2} \right\rangle \left\langle \frac{\partial U_3}{\partial x_2} \right\rangle x_2, \\ \langle U_3 \rangle \langle W_3 \rangle = - \langle U_3 \rangle \left\langle \frac{\partial U_1}{\partial x_2} \right\rangle \approx - \left\langle \frac{\partial U_1}{\partial x_2} \right\rangle \left\langle \frac{\partial U_3}{\partial x_2} \right\rangle x_2. \end{aligned}\right\} \tag{2.3}$$

Figure 2 gives the fluctuating helicity $\langle h \rangle$. The distribution of $\langle h \rangle$ is similar to that of H but has a shorter positive range. With rotation becoming stronger, the maxima of the helicity shift towards lower locations. In contrast, as Re_τ increases, the fluctuating helicity is reduced. The decomposed fluctuating helicity $\langle h_i \rangle$ of ST30 is shown in figure 2(*b*). When $x_2 \lessapprox 4$, $\langle h_1 \rangle \approx -\langle h_3 \rangle$, which can be deduced in a way similar to (2.3). Furthermore, $\langle h_2 \rangle$ is one order less than the other two components. Above the buffer layer, the three components are all negative.

Figure 3 shows the relation between the peak position $x_2^+|_{max[\langle h \rangle^+]}$ and the parameter Re_τ/Ro_τ. As Ro_τ increases or Re_τ decreases, the peaks approach the wall. Especially,

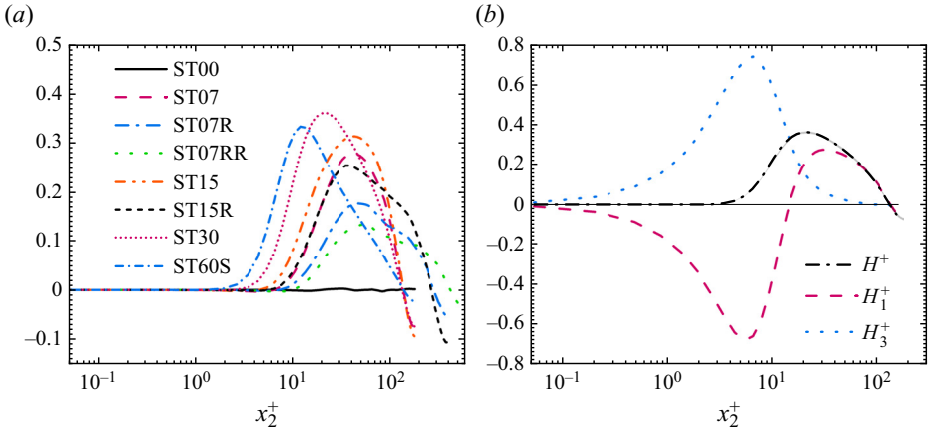

Figure 1. Profile of mean helicity: (*a*) overall helicity H^+; (*b*) decomposed helicity H_i^+ of ST30 and the grey filled region shows the error bar of H^+.

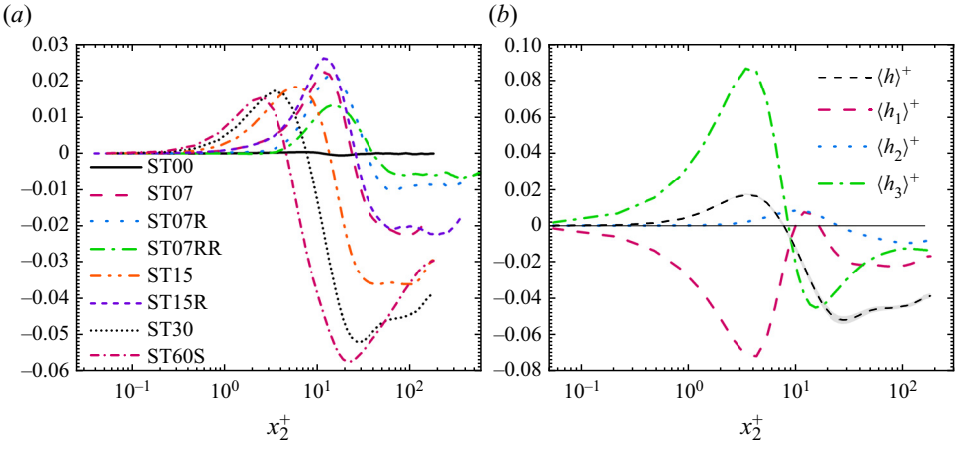

Figure 2. Profile of fluctuating helicity: (*a*) overall helicity $\langle h\rangle$; (*b*) decomposed helicity $\langle h_i\rangle$ of ST30 and the grey filled region shows the error bar of $\langle h\rangle^+$.

ST07 and ST15R have the same Re_τ/Ro_τ, and their peaks almost overlap with each other. The relation between the peak positions and the parameter Re_τ/Ro_τ is fitted using a sigmoid function, leading to the following expression:

$$x_2^+|_{\max[\langle h\rangle^+]} = 2.061/(0.1316 + \exp(-0.1218\, Re_\tau/Ro_\tau)). \tag{2.4}$$

In terms of the underlying mechanisms, as shown by the N–S equations (2.1), the Coriolis effects is proportional to the rotation rates Ω. As Ro_τ increases, rotation effects could penetrate deeper regions within the boundary layer. Considering the effects of Re_τ, for the near-wall inclined vortex structures, the streamwise velocity and the rotation-induced spanwise velocity are two opposing effects (Hu *et al.* 2023), which could be the same for the helicity. The streamwise velocity effects can be reflected through Re_τ. In the following analysis, the mechanism will be further discussed using the helicity budgets and structure functions.

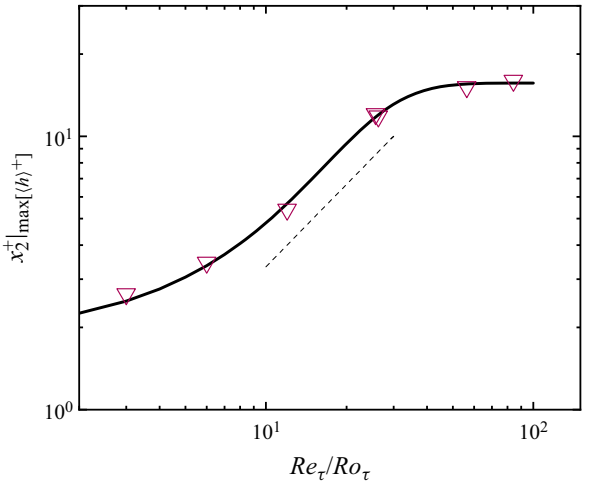

Figure 3. Relation between the peak $x_2^+|_{max[\langle h\rangle^+]}$ and the parameter Re_τ/Ro_τ. The black solid line is the fitted sigmoid function (2.4) and the black dashed line serves as a reference for the linear law.

2.2. *Helicity budget*

The budget equation for $\langle h\rangle$ is written as

$$-\langle\gamma_{i2}\rangle\frac{\mathrm{d}\langle U_i\rangle}{\mathrm{d}x_2}-\langle u_iu_2\rangle\frac{\mathrm{d}\langle W_i\rangle}{\mathrm{d}x_2}-\frac{\mathrm{d}\langle hu_2\rangle}{\mathrm{d}x_2}+\frac{1}{2}\frac{\mathrm{d}}{\mathrm{d}x_2}\langle u_iu_i\omega_2\rangle-\frac{1}{\rho}\frac{\mathrm{d}\langle\omega_2p_R\rangle}{\mathrm{d}x_2}-\frac{1}{\rho}\frac{\mathrm{d}\langle\omega_2p_T\rangle}{\mathrm{d}x_2}$$
$$+\nu\frac{\mathrm{d}^2\langle h\rangle}{\mathrm{d}x_2^2}-2\nu\left\langle\frac{\partial u_i}{\partial x_j}\frac{\partial\omega_i}{\partial x_j}\right\rangle+2\Omega\epsilon_{ij1}\langle u_j\omega_i\rangle=0, \tag{2.5}$$

where $\gamma_{ij}=\omega_iu_j-\omega_ju_i$ is the helical stress, and p_R and p_T are the decomposed pressure related to the Coriolis terms and the turbulent convection, respectively (Yang *et al.* 2020*a*; Hu, Li & Yu 2022*a*).

For the helical stress $\langle\gamma_{ij}\rangle$, the following relations can be derived:

$$\langle\gamma_{12}\rangle=\frac{\mathrm{d}}{\mathrm{d}x_2}\langle u_2u_3\rangle\,,\quad -\langle\gamma_{32}\rangle=\frac{\mathrm{d}}{\mathrm{d}x_2}\langle u_1u_2\rangle\,. \tag{2.6a,b}$$

That is, partial components of $\langle\gamma_{ij}\rangle$ can be represented by the wall-normal gradients of the Reynolds stresses. According to (2.6*a*,*b*), the production and the Coriolis term can be simplified, and the fluctuating helicity budget equation (FHE) can be rewritten as

$$\underbrace{-\frac{\mathrm{d}\langle u_2u_3\rangle}{\mathrm{d}x_2}\frac{\mathrm{d}\langle U_1\rangle}{\mathrm{d}x_2}+\frac{\mathrm{d}\langle u_1u_2\rangle}{\mathrm{d}x_2}\frac{\mathrm{d}\langle U_3\rangle}{\mathrm{d}x_2}-\langle u_iu_2\rangle\frac{\mathrm{d}\langle W_i\rangle}{\mathrm{d}x_2}}_{\langle\Pi\rangle}\underbrace{-\frac{\mathrm{d}\langle hu_2\rangle}{\mathrm{d}x_2}+\frac{1}{2}\frac{\mathrm{d}}{\mathrm{d}x_2}\langle u_iu_i\omega_2\rangle}_{\langle T\rangle}$$
$$\underbrace{-\frac{1}{\rho}\frac{\mathrm{d}\langle\omega_2p_R\rangle}{\mathrm{d}x_2}}_{\langle G_R\rangle}\underbrace{-\frac{1}{\rho}\frac{\mathrm{d}\langle\omega_2p_T\rangle}{\mathrm{d}x_2}}_{\langle G_T\rangle}+\underbrace{\nu\frac{\mathrm{d}^2\langle h\rangle}{\mathrm{d}x_2^2}}_{\langle D\rangle}\underbrace{-2\nu\left\langle\frac{\partial u_i}{\partial x_j}\frac{\partial\omega_i}{\partial x_j}\right\rangle}_{-\langle E\rangle}+\underbrace{2\frac{\mathrm{d}\langle u_1u_2\rangle}{\mathrm{d}x_2}\Omega}_{\langle C\rangle}=0, \tag{2.7}$$

where $\langle \Pi \rangle$ is the production and represents the interaction between the mean and fluctuating fields, $\langle T \rangle$ is the spatial turbulent convection, $\langle G_R \rangle$ and $\langle G_T \rangle$ are the pressure transfer terms related to the rotation effect and turbulent convection, $\langle D \rangle$ is the spatial viscous diffusion, $\langle E \rangle$ is the pseudo-dissipation, and $\langle C \rangle$ is the Coriolis term. Here, $\langle G \rangle = \langle G_T \rangle + \langle G_R \rangle$ is the total pressure transfer term. As shown in the equation, the Coriolis force directly affects the helicity distribution. Specifically, $\int_{-1}^{0} \langle C \rangle \, \mathrm{d}x_2 = 0$. The Coriolis term is a transfer term similar to the turbulent convection. This is non-trivial, because in the budget equation of the turbulent kinematic energy (TKE) and the GKE, the Coriolis term is zero and only redistributes energy among three components of TKE (Yang & Wang 2018). The direct effects of $\langle C \rangle$ on the fluctuating helicity imply that in addition to the TKE, $\langle h \rangle$ could be another important quantity in the dynamics of the streamwise-rotating channel turbulence.

The results of the FHE are given in figure 4. The production $\langle \Pi \rangle$ is mainly negative. There are mainly two mechanisms: the coupling effects between the helical stresses and the mean velocity gradients, and those between the Reynolds stresses and the mean vorticity gradients. The near-wall behaviour analyses in Appendix B.1 indicate that the first mechanism is dominant in the viscous sublayer. In fact, numerical results suggest that the first mechanism $(-\langle \gamma_{i2} \rangle \, \mathrm{d}\langle U_i \rangle / \mathrm{d}x_2)$ is always dominant, which is not shown here. The term in fact extracts positive fluctuating helicity to the mean helicity. The spatial turbulent convection $\langle T \rangle$ is mainly induced by convection $(-\mathrm{d}\langle h u_2 \rangle)$ and vortex deformation $(\mathrm{d}\langle u_i u_i \omega_2 \rangle / \mathrm{d}x_2/2)$. The term extracts positive helicity from the buffer layer to higher layers. Similarly, the viscous diffusion $\langle D \rangle$ transfers the positive helicity from the buffer layer and the high viscous sublayer towards the wall. Different from the pseudo-dissipation of energy, the helicity pseudo-dissipation $\langle E \rangle$ is not positive-definite. It is positive in the vicinity of the wall but negative at higher wall-normal positions. The Coriolis term $\langle C \rangle$ and the pressure term $\langle G \rangle$ are the two direct effects induced by rotation. In streamwise-rotating channel turbulence, the profile of the Reynolds stress $\langle u_1 u_2 \rangle$ is approximately not affected by rotation (Yang & Wang 2018). According to the definition of the Coriolis term and the profile of Reynolds stress $\langle u_1 u_2 \rangle$, it could be inferred that the term is negative around the wall but positive around the channel centre. The term transfers positive helicity from the buffer layer toward the higher layers. In contrast, the pressure term $\langle G \rangle$ transfers positive helicity from the channel centre toward the wall. The term is induced by the turbulent convection $\langle G_T \rangle$ and the Coriolis force $\langle G_R \rangle$. According to the Green function of the pressure Poisson equation (Kim 1989), the pressure always has the opposite values with its origin (convection or rotation) (Yang & Wang 2018; Yang *et al.* 2018). In fact, since there is no fluctuating helicity in non-rotating channel turbulence, the Coriolis term and the corresponding pressure transfer term are the direct reasons for the non-zero fluctuating helicity. However, the Coriolis term has the opposite sign with the fluctuating helicity, especially for ST07. The rotation-induced pressure transfer terms could be the main source for the fluctuating helicity.

Figure 5 shows the distribution of $\langle G_R \rangle$, $\langle C \rangle$ and $\langle T \rangle$ for different cases. As shown, the two terms $\langle G_R \rangle$ and $\langle C \rangle$ are both proportional to Ro_τ, while their relationship with Re_τ remains less evident. In comparison, the turbulent convection $\langle T \rangle$ is increased by both Ro_τ and Re_τ. Especially, the comparison between ST15 and ST15R indicates that the Reynolds number effects are more remarkable for $\langle T \rangle$. These findings suggest that the contrasting impacts of Re_τ and Ro_τ on the peak law (2.4) might be associated with the terms $\langle T \rangle$ and $\langle G_R \rangle + \langle C \rangle$, respectively.

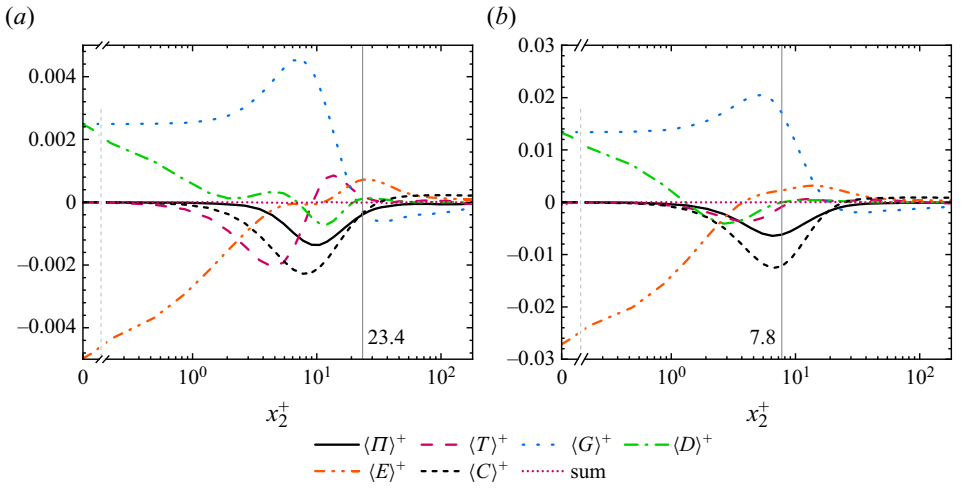

Figure 4. Fluctuating helicity budget: (*a*) ST07; (*b*) ST30. The black solid lines of $x_2^+ = 23.4$ and $x_2^+ = 7.8$ give the zeros points of the helicity distribution in figure 2(*a*).

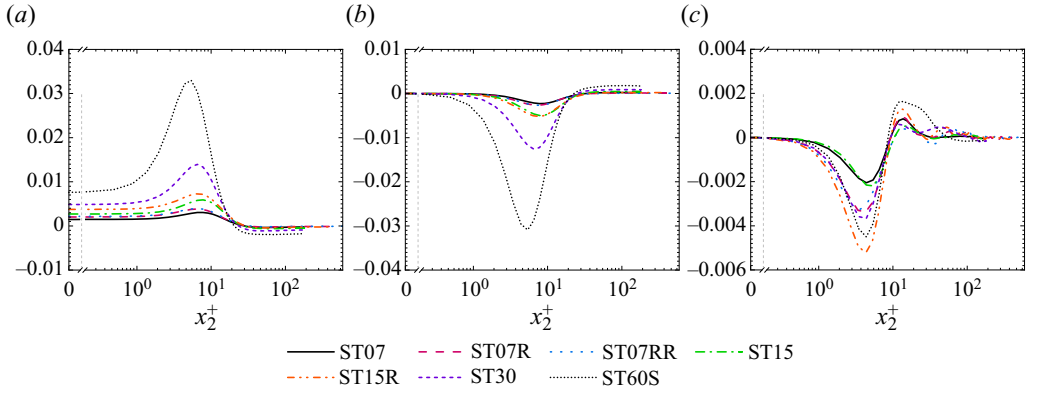

Figure 5. (*a*) $\langle G_R \rangle$, (*b*) $\langle C \rangle$ and (*c*) $\langle T \rangle$ of different cases in the helicity budget.

In addition, the near-wall behaviours of all terms in the helicity budget are estimated in Appendix B.1:

$$\left.\begin{aligned} |\langle \Pi \rangle^+| \sim x_2^{+2}, \quad |\langle T \rangle^+| \sim x_2^{+2}, \quad |\langle G \rangle^+| \sim 1, \\ |\langle D \rangle^+| \sim 1, \quad |\langle E \rangle^+| \sim 1, \quad |\langle C \rangle^+| \sim x_2^{+2}, \end{aligned}\right\} \tag{2.8}$$

which is verified in figure 6. Especially, on the wall, there is a relation between the pressure transfer and viscous effects:

$$\langle G \rangle^+\big|_{x_2=\pm h} = \langle D \rangle^+\big|_{x_2=\pm h} = \tfrac{1}{2}\,\langle E \rangle^+\big|_{x_2=\pm h}, \tag{2.9}$$

which means that the total pressure transfer is equal to the viscous diffusion on the wall. The relation is proved in Appendix B.2.

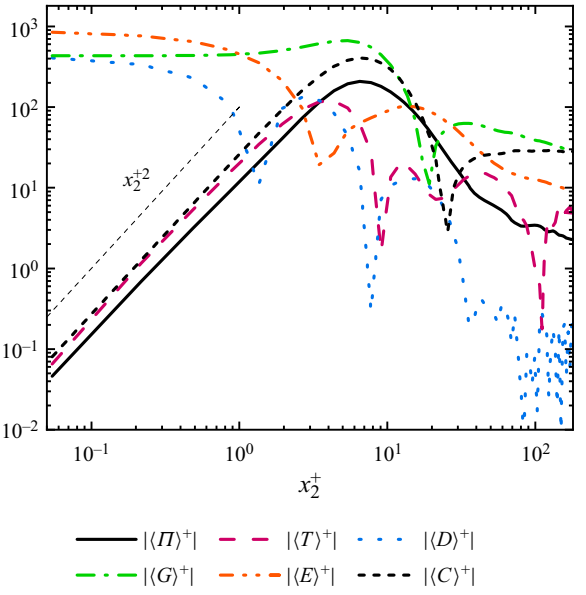

Figure 6. Near-wall behaviours of helicity budget of ST30.

3. Differentiated generalized Kolmogorov equation of helicity

According to the multiscale property of turbulence, the interscale dynamics are as important as the spatial ones. In this section, our focus lies on examining the distribution of scale helicity and its corresponding budget equation, thereby elucidating the multiscale behaviours of helicity and several crucial physical processes.

3.1. *Scale helicity distribution*

First, we want to explain the relation between structure function and Fourier spectrum. Taking the scale energy for example (Davidson 2015), supposing the energy spectrum gives the exact definition of the energy at specific scale, one-dimensional Fourier transformation leads to the conclusion that the second-order structure function represents all energy in eddies of size r or less plus a term related to the enstrophy in eddies of size r or greater. However, since eddies of given size contribute to the energy spectrum across the full range of wavenumbers, the energy spectrum is not the exact definition of scale helicity. Therefore, for simplicity, one can also believe that the second-order structure function for energy (helicity) represents all energy (helicity) in eddies of size r or less.

To get the helicity at a given scale, differentiation with respect to the scale r is needed. Since the streamwise direction is strongly affected by rotation (Yang & Wang 2018), in this paper, the focus is on the interscale dynamics in the x_1 direction. The scale helicity is then defined as

$$\langle \delta h \rangle (X_2, r_1) = \left\langle \partial_{r_1} (\delta u_i(\boldsymbol{X}, r_1) \delta \omega_i(\boldsymbol{X}, r_1)) \right\rangle, \tag{3.1}$$

where δ means the increment of a quantity at two positions, $\boldsymbol{X} = (\boldsymbol{x} + \boldsymbol{x}')/2$ is the centre of the two positions, r_1 is the streamwise component of $\boldsymbol{r}$ and $\boldsymbol{r} = (\boldsymbol{x} - \boldsymbol{x}')$ is the scale vector. Specifically, the velocity and the vorticity increments between the two positions $\boldsymbol{x}$

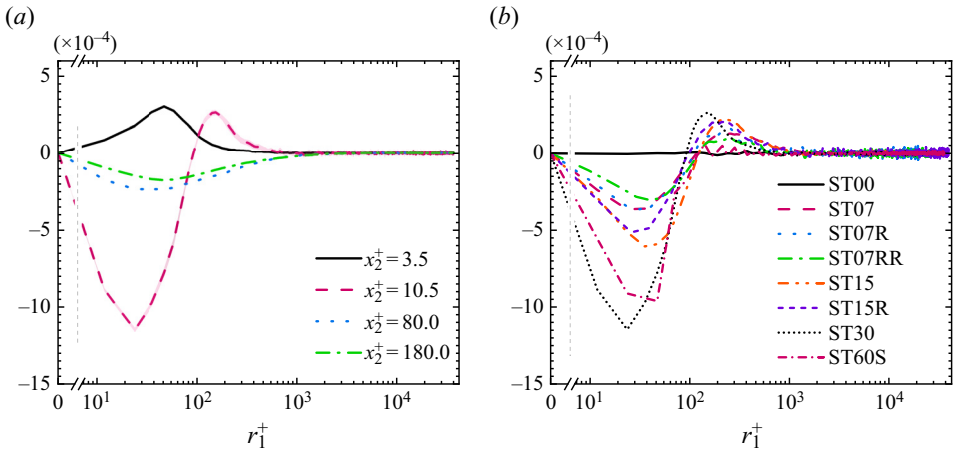

Figure 7. Scale helicity distribution: (*a*) $\langle \delta h \rangle$ of ST30, and the pink filled region shows the error bar of $\langle \delta h \rangle$ in the buffer layer $x_2^+ = 10.5$; (*b*) $\langle \delta h \rangle$ in the buffer layer ($x_2^+ = 10.3$ for ST07R and ST15R, $x_2^+ = 10.0$ for ST07RR and $x_2^+ = 10.5$ for the other cases).

and $\boldsymbol{x}'$ are defined as

$$\delta u_i(\boldsymbol{X}, r_1) = u_i(\boldsymbol{x}) - u_i(\boldsymbol{x}'), \quad \delta\omega_i(\boldsymbol{X}, r_1) = \omega_i(\boldsymbol{x}) - \omega_i(\boldsymbol{x}'). \tag{3.2a,b}$$

The streamwise scale helicity $\langle \delta h \rangle (X_2, r_1)$ is shortened as $\langle \delta h \rangle$ hereafter. When r_1 tends to infinity, the integral of the scale helicity tends to 2 times the fluctuating helicity:

$$\lim_{r_1 \to \infty} \int_0^{r_1} \langle \delta h \rangle \, (X_2, l_1) \, \mathrm{d}l_1 = \lim_{r_1 \to \infty} \left\langle (u_i - u_i')(\omega_i - \omega_i') \right\rangle = 2 \, \langle u_i \omega_i \rangle \, , \tag{3.3}$$

which supports our definition about the scale helicity.

Figure 7(*a*) shows the scale helicity distribution of ST30 at different positions. As shown, the distribution at $x_2^+ = 10.5$ is negative at small scales ($r_1^+ \lessapprox 10^2$) but positive at larger scales ($r_1^+ \gtrapprox 10^2$), consistent with the observation of Yu *et al.* (2022). It means that from the wall towards the channel centre, the small-scale helicity first changes from positive to negative. The change of large-scale helicity happens at a higher wall-normal position. The comparison of different cases in the buffer layer is shown in figure 7(*b*). As Ro_τ increases from 0 to 30, the small-scale helicity has a larger negative value. With continued intensification of rotation, the small-scale helicity slightly decreases and the large-scale positive helicity completely diminishes. It means that the scale helicity changes its signs at lower wall-normal positions. In contrast, as Re_τ increases, the scale helicity slightly decreases.

Similarly, the scale distribution of the pressure is defined as

$$\left\langle \delta p^2 \right\rangle (X_2, r_1) = \left\langle \partial_{r_1} (\delta p(\boldsymbol{X}, r_1) \delta p(\boldsymbol{X}, r_1)) \right\rangle . \tag{3.4}$$

The decomposed scale pressures $\langle \delta p_R^2 \rangle$ and $\langle \delta p_T^2 \rangle$ are defined in the same way. Figure 8 displays the normalized scale pressure and its decomposition of ST30. As shown, p_R has a larger streamwise length scale than p and p_T, which can be inferred from the Poisson equation of the decomposed pressures (Yang *et al.* 2018).

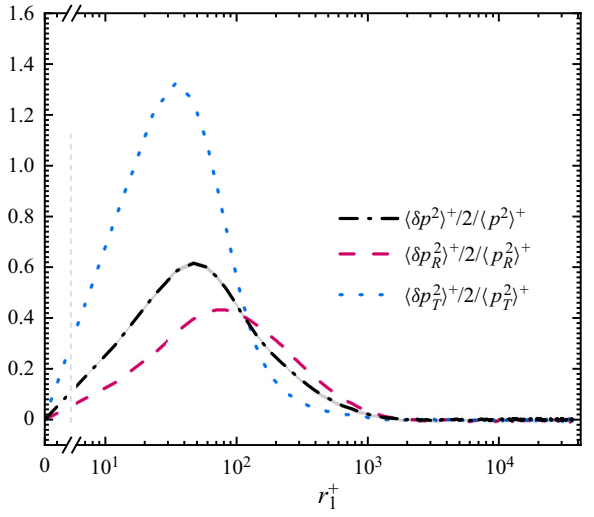

Figure 8. Scale distribution of the pressure and its decomposition of ST30 non-dimensionalized using the corresponding mean-square value in the buffer layer $x_2^+ = 10.5$. The grey filled region shows the error bar of $\langle \delta p^2 \rangle/2/\langle p^2 \rangle$.

3.2. *DHGKE analysis*

To analyse the interscale dynamics in channel turbulence, the GKE was used by Marati *et al.* (2004) and Cimarelli *et al.* (2013, 2015, 2016). In the present study, the interscale dynamics in the streamwise-rotating channel turbulence are investigated from the perspective of scale helicity through corresponding budgets, which is named as the differentiated generalized Kolmogorov equation for helicity (DHGKE) hereafter. Deduced from the N–S equation, with the assumption $\langle U_2 \rangle = \langle W_2 \rangle = 0$, $\boldsymbol{\Omega} = \Omega \boldsymbol{e}_1$, DHGKE is written as

$$\begin{aligned}
\underbrace{\frac{\partial}{\partial r_1}\frac{\partial}{\partial t}\delta u_i \delta \omega_i}_{\Delta_t} = {} & \underbrace{-\frac{\partial}{\partial r_1}\delta u_i \delta u_j \frac{\mathrm{d}\langle W_i^* \rangle}{\mathrm{d}X_j} - \frac{\partial}{\partial r_1}(\delta \omega_i \delta u_j - \delta u_i \delta \omega_j)\frac{\mathrm{d}\langle U_i^* \rangle}{\mathrm{d}X_j}}_{\Pi^S} \\
& \underbrace{-\frac{\partial}{\partial r_1}\frac{\partial}{\partial r_j}(\delta h \delta u_j) + \frac{1}{2}\frac{\partial}{\partial r_1}\frac{\partial}{\partial r_j}(\delta \omega_j \delta u^2)}_{T^{SS}} \underbrace{-\frac{\partial}{\partial r_1}\frac{\partial}{\partial X_j}(u_j^* \delta h) + \frac{1}{2}\frac{\partial}{\partial r_1}\frac{\partial}{\partial X_j}(\delta u^2 \omega_j^*)}_{T^{SP}} \\
& \underbrace{-\frac{1}{\rho}\frac{\partial}{\partial r_1}\frac{\partial}{\partial X_j}(\delta \omega_j \delta p_T)}_{G_T^S} \underbrace{-\frac{1}{\rho}\frac{\partial}{\partial r_1}\frac{\partial}{\partial X_j}(\delta \omega_j \delta p_R)}_{G_R^S} + \underbrace{2\nu \frac{\partial}{\partial r_1}\frac{\partial^2(\delta h)}{\partial r_j \partial r_j}}_{D^{SS}} + \underbrace{\frac{\nu}{2}\frac{\partial}{\partial r_1}\frac{\partial^2(\delta h)}{\partial X_j \partial X_j}}_{D^{SP}} \\
& \underbrace{-4\frac{\partial}{\partial r_1}\epsilon^{H*}}_{-E^S} + \underbrace{2\Omega \frac{\partial}{\partial r_1}\left(\delta \omega_2 \delta u_3 - \delta u_2 \delta \omega_3 + \delta u_k \delta \frac{\partial u_k}{\partial x_1}\right)}_{C^S},
\end{aligned} \tag{3.5}$$

where $*$ represents the average at the two positions $\boldsymbol{x}$ and $\boldsymbol{x}'$, Δ_t is the time derivatives, Π^S is the production, T^{SS} is the interscale turbulent convection, T^{SP} is the spatial turbulent convection, G_R^S and G_T^S are the pressure transfer terms related to the rotation effects and

turbulent convection, D^{SS} is the interscale viscous diffusion, D^{SP} is the spatial viscous diffusion, E^S is the pseudo-dissipation, and C^S is the Coriolis transfer term. Here, $G^S = G_T^S + G_R^S$ is the total pressure transfer term.

If averaging over the $x_1 - x_3$ plane, using the relation $\partial/\partial X_1\langle\cdot\rangle = \partial/\partial X_3\langle\cdot\rangle = 0$ and $\partial/\partial t = 0$, DHGKE can be written as

$$\underbrace{-\frac{\partial}{\partial r_1}\langle\delta u_i\delta u_2\rangle\frac{\mathrm{d}\langle W_i^*\rangle}{\mathrm{d}X_2} - \frac{\partial}{\partial r_1}\langle\delta\omega_i\delta u_2 - \delta u_i\delta\omega_2\rangle\frac{\mathrm{d}\langle U_i^*\rangle}{\mathrm{d}X_2}}_{\langle\Pi^S\rangle} \underbrace{-\frac{\partial}{\partial r_1}\frac{\partial}{\partial r_j}\langle\delta h\delta u_j\rangle + \frac{1}{2}\frac{\partial}{\partial r_1}\frac{\partial}{\partial r_j}\langle\delta\omega_j\delta u^2\rangle}_{\langle T^{SS}\rangle}$$
$$\underbrace{-\frac{\partial}{\partial r_1}\frac{\partial}{\partial X_2}\langle u_2^*\delta h\rangle + \frac{1}{2}\frac{\partial}{\partial r_1}\frac{\partial}{\partial X_2}\langle\delta u^2\omega_2^*\rangle}_{\langle T^{SP}\rangle} \underbrace{-\frac{1}{\rho}\frac{\partial}{\partial r_1}\frac{\partial}{\partial X_2}\langle\delta\omega_2\delta p_T\rangle}_{\langle G_T^S\rangle} \underbrace{-\frac{1}{\rho}\frac{\partial}{\partial r_1}\frac{\partial}{\partial X_2}\langle\delta\omega_2\delta p_R\rangle}_{\langle G_R^S\rangle}$$
$$\underbrace{+2\nu\frac{\partial}{\partial r_1}\frac{\partial^2\langle\delta h\rangle}{\partial r_j\partial r_j}}_{\langle D^{SS}\rangle} \underbrace{+\frac{\nu}{2}\frac{\partial}{\partial r_1}\frac{\partial^2\langle\delta h\rangle}{\partial X_2^2}}_{\langle D^{SP}\rangle} \underbrace{+2\Omega\frac{\partial}{\partial r_1}\frac{\partial}{\partial X_2}\langle\delta u_2\delta u_1\rangle}_{\langle C^S\rangle} = 0. \tag{3.6}$$

Similar to the GKE results given by Marati *et al.* (2004) and the limited behaviours in (3.3), when $r_1 \to \infty$, there are also relations for the spatial and interscale transfer terms:

$$\left.\begin{aligned}\lim_{r_1\to\infty}\int_0^{r_1}\left\langle D^{SS}\right\rangle(X_2, l_1)\,\mathrm{d}l_1 &= \lim_{r_1\to\infty}\int_0^{r_1}\left\langle D^{SP}\right\rangle(X_2, l_1)\,\mathrm{d}l_1,\\ \lim_{r_1\to\infty}\int_0^{r_1}\left\langle T^{SS}\right\rangle(X_2, l_1)\,\mathrm{d}l_1 &= \lim_{r_1\to\infty}\int_0^{r_1}\left\langle T^{SP}\right\rangle(X_2, l_1)\,\mathrm{d}l_1.\end{aligned}\right\} \tag{3.7}$$

DHGKE results of ST07 and ST30 in the viscous sublayer ($x_2^+ = 3.5$) are shown in figures 9(*a*) and 9(*b*), respectively. As shown in figure 9(*a*), the pressure terms $\langle G_R^S\rangle$ and $\langle G_T^S\rangle$ are the main positive sources for the scale helicity. The interscale viscous diffusion $\langle D^{SS}\rangle$ transfers positive helicity from $r_1^+ \sim 100$ to smaller scales ($r_1^+ \sim 20$). In contrast, the spatial viscous diffusion $\langle D^{SP}\rangle$ is mainly negative and transfers positive scale helicity to higher wall-normal position. Consistent with the helicity budget in figure 4, the production $\langle\Pi^S\rangle$ and the Coriolis term $\langle C^S\rangle$ are both negative here and restrain the scale helicity in the viscous sublayer. The spatial and interscale turbulent convections $\langle T^{SP}\rangle$ and $\langle T^{SS}\rangle$ are also negative. Generally, for energy transfer in streamwise-rotating channel turbulence (Yang & Wang 2018), the pressure transfers are negligible. However, the pressure transfers are the main sources for the scale helicity here, while other terms except for $\langle D^{SS}\rangle$ suppress the development of the scale helicity. Figure 9(*b*) gives the DHGKE results of ST30. The amplitudes of all terms increase with rotation rates. Compared with other terms, the convection-induced pressure term $\langle G_T^S\rangle$ is strengthened. Additionally, the distribution of the interscale turbulent convection $\langle T^{SS}\rangle$ is completely changed. The term transfers positive helicity towards small scales. Relatively, $\langle D^{SS}\rangle$, $\langle D^{SP}\rangle$ and $\langle T^{SP}\rangle$ are weaker in ST30 than in ST07. It is because that $\langle C^S\rangle$ and $\langle G_R^S\rangle$ are defined to be proportional to the rotation rates, while the other turbulent processes are not.

Figure 10 shows the results in the buffer layer ($x_2^+ = 10.5$). For ST07, most terms have a similar distribution as those in the viscous sublayer. However, the spatial viscous diffusion $\langle D^{SP}\rangle$ is negligible in this layer. Here, $\langle T^{SS}\rangle$ is more important and transfers positive

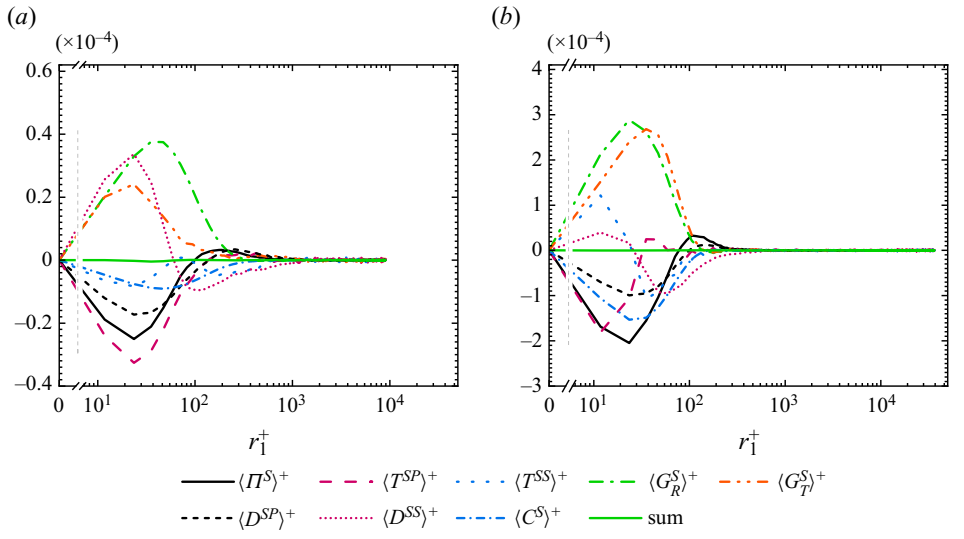

Figure 9. DHGKE in the viscous sublayer ($x_2^+ = 3.5$): (*a*) ST07; (*b*) ST30.

helicity towards smaller scales. Most importantly, the production term $\langle \Pi^S \rangle$ is dominant in this layer and its peak locates on $r_1^+ \approx 30$. Notably, as shown in figure 7(*b*), the scale helicity in this layer is negative when $r_1^+ \lessapprox 100$ but positive when r_1^+ is larger, and its negative peaks also locate on $r_1^+ \approx 30$. This implies that the production term is the main term inducing the sign change of the scale helicity. Similarly, $\langle T^{SP} \rangle$ is negative at small scales but positive at large scales, and could also be related to the scale discrepancy of the scale helicity distribution, even if its negative peak locates at a smaller scale ($r_1^+ \approx 20$). Therefore, $\langle \Pi^S \rangle$ and $\langle T^{SP} \rangle$ are the core effects of the mean flow and spatial turbulent convection on the small-scale negative helicity. In contrast, the interscale transfer terms $\langle D^{SS} \rangle$ and $\langle T^{SS} \rangle$ are positive at small scales but negative at large scales. These two terms cascade positive scale helicity to small scales and cancel the imbalance of chirality. The behaviours of $\langle T^{SS} \rangle$ are far different from the findings in homogeneous turbulence, where only the prevalence of a single chirality is considered (Mininni & Pouquet 2009, 2010; Mininni, Rosenberg & Pouquet 2012; Hu, Li & Yu 2022*b*). DHGKE results of ST30 in figure 10(*b*) are more concise than those of ST07. Here, $\langle T^{SP} \rangle$, $\langle G_T^S \rangle$ and $\langle D^{SP} \rangle$ are negligible, while other terms have the same distribution as those of ST07. The results of ST30 highlight the effects of the mean flow gradients on the discrepancy between small- and large-scale helicity.

To further discuss the mechanisms related to the peak laws (2.4), figure 11(*a–d*) shows the effects of Re_τ and Ro_τ on $\langle \Pi^S \rangle$, $\langle T^{SS} \rangle$, $\langle G_R^S \rangle$ and $\langle C^S \rangle$, respectively, around the peaks ($x_2^+ \approx 5.4$). As shown, the production $\langle \Pi^S \rangle$, the Coriolis term $\langle C^S \rangle$ and corresponding pressure term $\langle G_R^S \rangle$ are remarkably proportional to the rotation rates, yet they remain unaffected by variations in the Reynolds number Re_τ. In contrast, Re_τ has the opposing effects with Ro_τ on the interscale turbulent convection $\langle T^{SS} \rangle$. Specifically, at $r_1^+ \sim 10$, $\langle T^{SS} \rangle$ exhibits a positive and amplified trend with the intensification of rotation, but becomes negative with increasing Re_τ. When summing over r_1^+, the positive values at small scales induced by rotation are partially counteracted by the negative values at large scales, while Re_τ merely enhances the negative amplitudes of $\int \langle T^{SS} \rangle \, \mathrm{d}r_1$. This reveals the

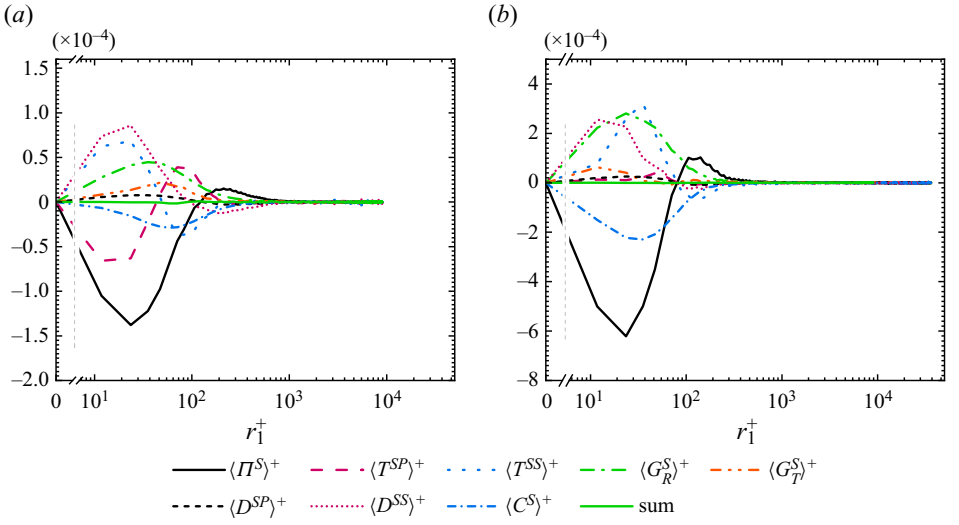

Figure 10. DHGKE in the buffer layer ($x_2^+ = 10.5$): (*a*) ST07; (*b*) ST30.

detailed opposing effects of Re_τ and Ro_τ on the peak laws (2.4) through the convection $\langle T^{SS}\rangle$ and rotation $\langle G_R^S\rangle + \langle C^S\rangle$.

The DHGKE results in the log-law layer ($x_2^+ = 80.0$) are shown in figure 12. As shown, even if 81 time slices with a time interval of 1 h/u_τ have been used to evaluate the data, the quality of results obtained from ST07 remains relatively poor. Additional error estimations are given in Appendix A.2. Since the results of ST30 are quite similar to those of ST07, the details of ST30 are discussed at first. As shown in figure 12(*b*), in this layer, similar to the TKE budget equation and GKE, the production $\langle \Pi^S\rangle$ is negligible, attributed to the gradients of mean velocities and vorticities. For the spatial effects, traditionally, in the log-law layer, the spatial energy transfers are also negligible (Marati *et al.* 2004). The physical process in the log-law layer is usually believed to be isolated from the spatial effects and is closely related to the turbulent dynamics in homogeneous turbulence. However, for the DHGKE here, the Coriolis term $\langle C^S\rangle$ and the rotation-induced pressure transfer term $\langle G_R^S\rangle$ are both spatial transfers. It concretely shows that the turbulent structures are strongly influenced by $\langle C^S\rangle$ and $\langle G_R^S\rangle$. The two effects exhibit opposing tendencies, akin to those observed in the Reynolds stress budget provided by Yang & Wang (2018). The positive $\langle C^S\rangle$ can be readily deduced from its spatial transfer property and the negative $\langle G_R^S\rangle$ can be inferred from the pressure Poisson equation (Kim 1989). In the log-law layer, $\langle T^{SS}\rangle$ cascades negative scale helicity to small scales. Since the main spatial effects locate on the largest scale and the scale helicity is always negative at this location, the interscale dynamics of helicity in the log-law layer are consistent with those of homogeneous turbulence. Similar to $\langle C^S\rangle$, $\langle T^{SP}\rangle$ is positive and transfers positive helicity from this layer towards the wall. The results of ST07 are similar to those of ST30, while the term $\langle G_T^S\rangle$ is not negligible. Figure 13 shows the Reynolds and rotation number effects on $\langle G_R^S\rangle$ and $\langle C^S\rangle$ in the log-law layer. As shown, with increasing rotation rates, the two terms usually become larger. In contrast, as Re_τ increases, the amplitudes of the two terms in the log-law layer decrease significantly, which can be linked to the vortex angles discussed in § 4.

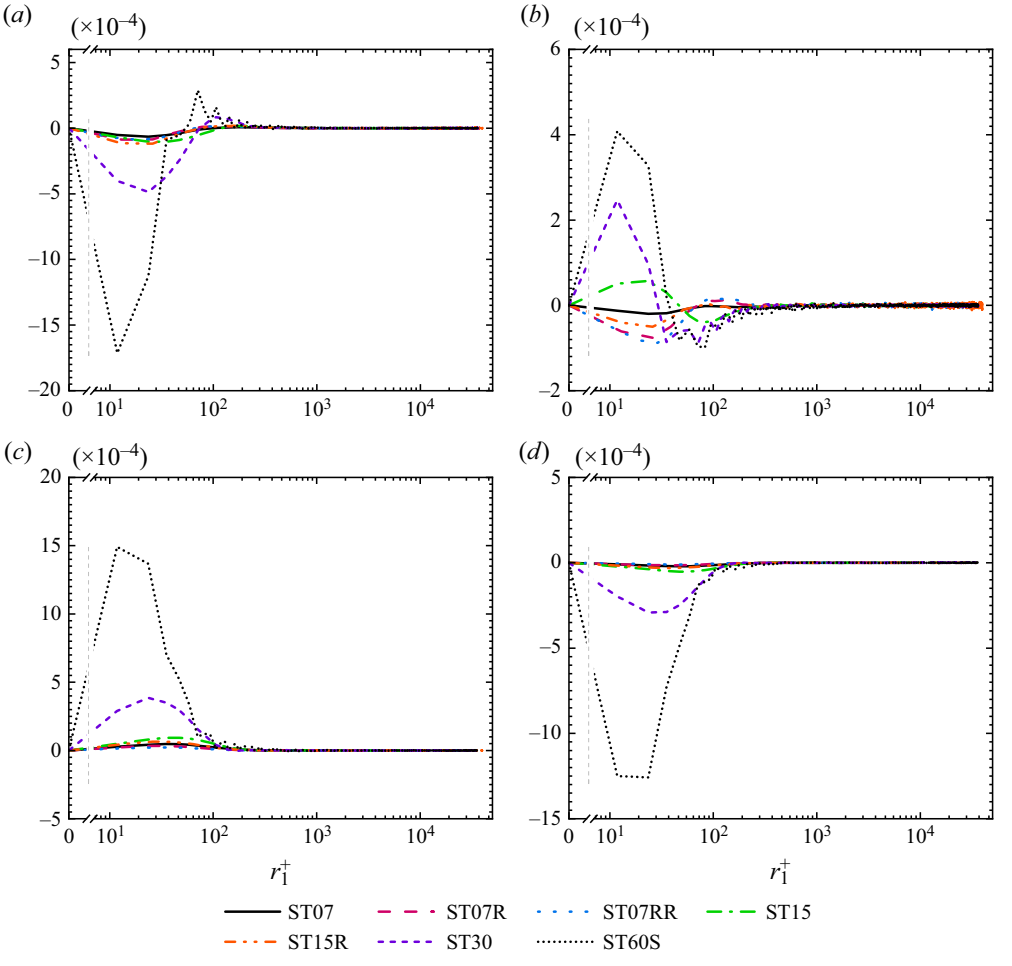

Figure 11. (*a*) $\langle \Pi^S \rangle$, (*b*) $\langle T^{SS} \rangle^+$, (*c*) $\langle G_R^S \rangle^+$ and (*d*) $\langle C^S \rangle^+$ for different cases around the peak of the fluctuating helicity ($x_2^+ = 5.3$ for ST07R and ST15R, $x_2^+ = 5.4$ for the other cases).

To further investigate the DHGKE results, the correlation factor for any two variables ζ and ξ (Baj, Portela & Carter 2022) is introduced:

$$\mathrm{corr}(\zeta, \xi) = \frac{\langle \zeta \xi \rangle - \langle \zeta \rangle \langle \xi \rangle}{\sqrt{\langle \zeta^2 \rangle - \langle \zeta \rangle^2} \sqrt{\langle \xi^2 \rangle - \langle \xi \rangle^2}}. \tag{3.8}$$

Figure 14 shows the correlation factor among the terms in the DHGKE of ST30 located at $x_2^+ = 3.5$ in figure 14(*a*), $x_2^+ = 10.5$ in figure 14(*b*,*d*) and $x_2^+ = 80.0$ in figure 14(*c*). Figure 14(*a–c*) is of the scale $r_1^+ = 47.1$, and figure 14(*d*) is of the scale $r_1^+ = 164.9$. The comparison between figures 14(*b*) and 14(*d*) shows that the results of $r_1^+ = 47.12$ are similar to those of $r_1^+ = 164.9$. In the viscous sublayer (figure 14*a*) and the buffer layer (figure 14*b*), the time derivative Δ_t is mainly proportional to the production Π^S, which is dominant in this layer. Additionally, in the log-law layer, the spatial and interscale turbulent convections T^{SP} and T^{SS} are the dominant terms. The term T^{SP} can be explained as the large-scale sweep effects (Baj *et al.* 2022). In addition, in the viscous sublayer

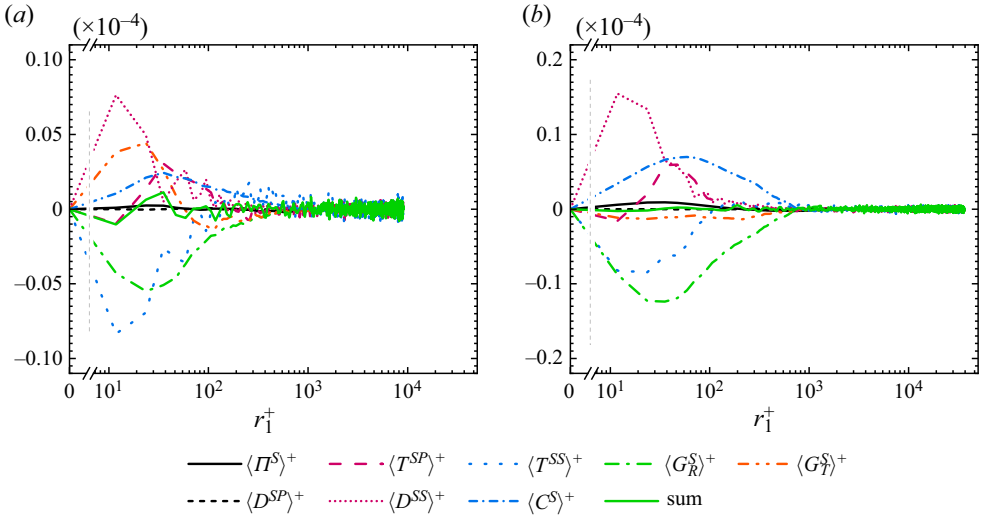

Figure 12. DHGKE in the log-law layer ($x_2^+ = 80.0$): (*a*) ST07; (*b*) ST30.

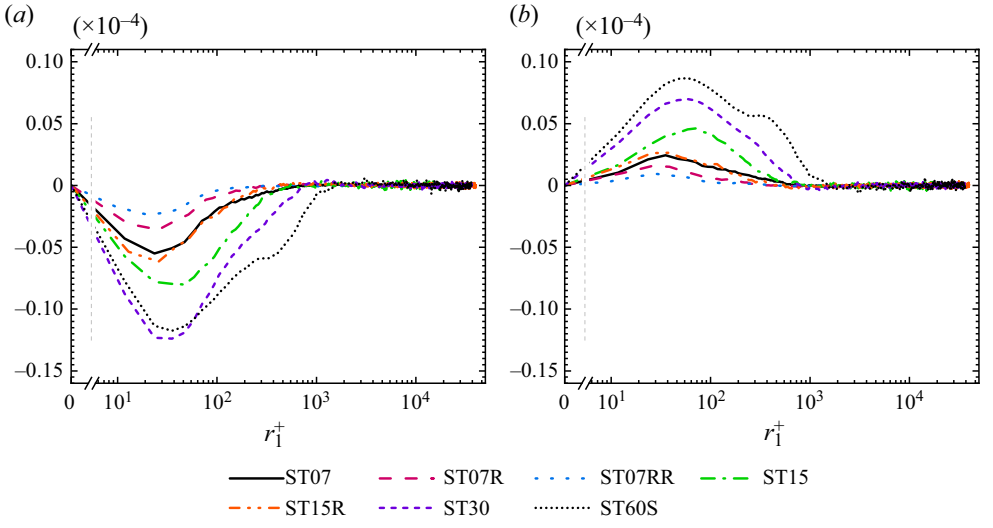

Figure 13. (*a*) G_R^{S+} and (*b*) C^{S+} for different cases in the log-law layer ($x_2^+ = 81.6$ for ST07R and ST15R, $x_2^+ = 80.3$ for ST07RR, $x_2^+ = 80.0$ for the other cases).

(figure 14*a*) and the buffer layer (figure 14*b*), T^{SP} and T^{SS} are anti-correlated. In contrast, in the buffer (figure 14*b*,*d*) and log-law layer (figure 14*c*), D^{SS} and D^{SP} are correlated. In Appendix C, the four effects are expanded in two-point correlation. The comparison between the expansions of D^{SP} and D^{SS} (or T^{SP} and T^{SS}) indicates that the two terms have the same sub-terms but different signs for every sub-term. Taking D^{SP} and D^{SS} for example, the positive correlation between the two terms can be explained by the prevalence of sub-terms with identical signs compared with those with opposing signs. Specifically, the sub-term $2(\partial u_i/\partial x_j)(\partial \omega_i'/\partial x_j') + 2(\partial u_i'/\partial x_j')(\partial \omega_i/\partial x_j)$ have opposing signs in the expansion of D^{SP} and D^{SS}, and could be related to the two-point correlation of the

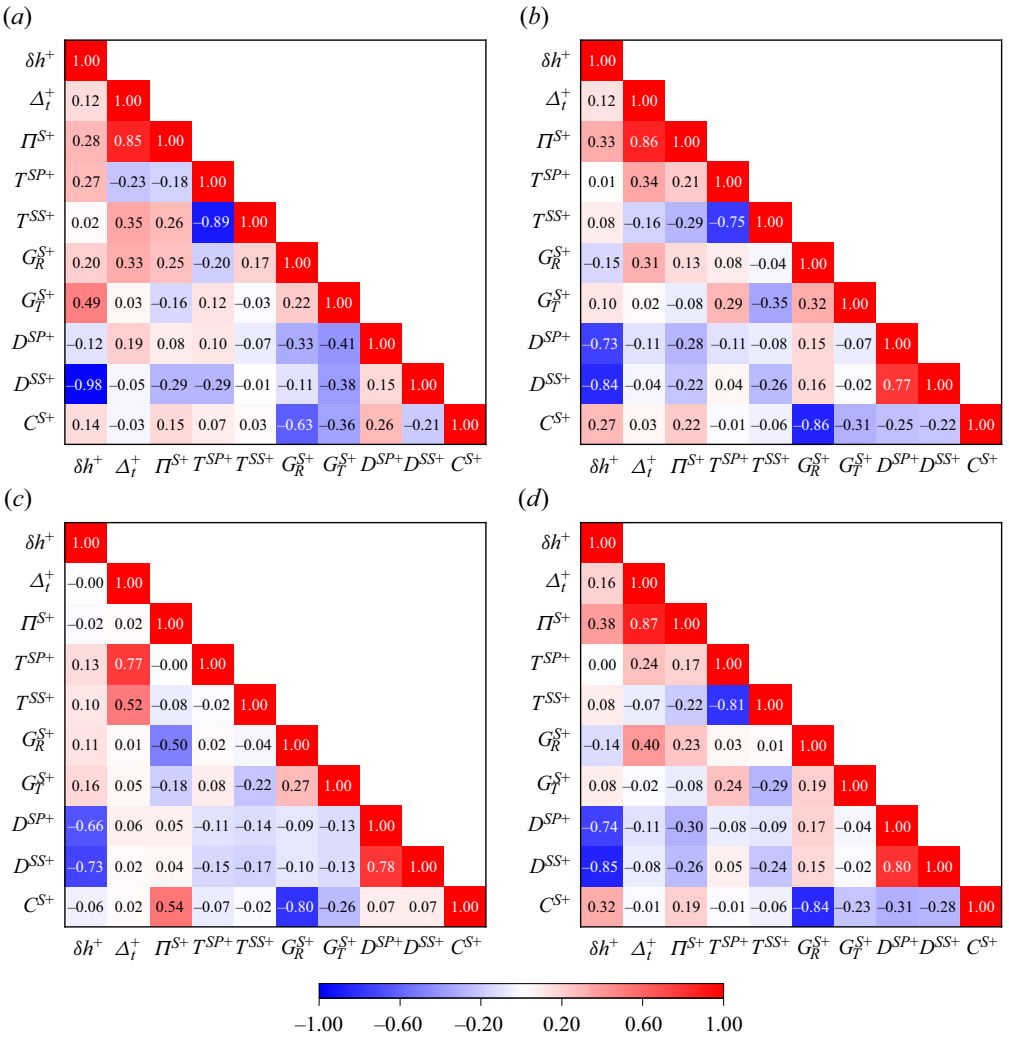

Figure 14. Correlation factor of all terms in the DHGKE in the (*a*) viscous sublayer ($x_2^+ = 3.5$), (*b*,*d*) buffer layer ($x_2^+ = 10.5$) and (*c*) log-law layer ($x_2^+ = 80.0$). Panels (*a–c*) present the results with the scale $r_1^+ = 47.1$ and panel (*d*) presents the results with the scale $r_1^+ = 164.9$.

pesudo-dissipation. The strong positive correlation between D^{SP} and D^{SS} above the buffer layer means the two-point correlation of the pesudo-dissipation is negligible compared with other sub-terms. Additionally, the anti-correlations between the Coriolis term C^S and corresponding pressure term G_R^S are also confirmed (Kim 1989; Yang *et al.* 2018). Here, C^S is also correlated with the production term Π^S, owing to the fact that, on average, C^S can be represented by the Reynolds stress $\delta u_1 \delta u_2$ (2.6*a*,*b*), which also presents in Π^S.

In conclusion, different from the scale energy dynamics, the two main effects for the scale helicity balance are the Coriolis term and corresponding pressure term. Therefore, helicity could directly reflect the effects of rotation. In the viscous sublayer, another main effect is the interscale viscous diffusion of the scale helicity towards small scales. In the buffer layer, the production and the spatial turbulent convection lead to the scale discrepancy of the scale helicity. The interscale turbulent convection reduces the

discrepancy between small- and large-scale helicity. Further studies around the peaks of helicity shows that the opposing effects of Re_τ and Ro_τ are mainly related to the turbulent convection and rotation effects (Coriolis term and corresponding pressure term), respectively. In the log-law layer, the negative scale helicity is found at all scales. The interscale turbulent convection has opposite sign with that in the buffer layer and cascades negative helicity towards small scales. Finally, using the correlation analysis, the large-scale sweep effects (Baj *et al.* 2022) and other basic results are confirmed. The consistency of the spatial and interscale effects are found and explained by the prevalence of different sub-terms in two-point correlation expansions.

4. Vortex structures

Vortex is an important topic in fluid dynamics. The streaks, streamwise vortices and hairpin vortices in the non-rotating channel turbulence have been studied by various researchers (Jiménez & Pinelli 1999; Wang, Huang & Xu 2015). In streamwise-rotating channel turbulence, previous studies mainly cared about the large-scale TG vortices (Yang & Wang 2018; Yan *et al.* 2022) and the inclined structures (Dai *et al.* 2019; Hu *et al.* 2023). In this study, the vortices are examined from a relatively microscopic perspective.

Figure 15 shows typical vortices in ST30 extracted through the Q criterion ($Q > 400$). On the vortices, the overall helicity h, the streamwise helicity h_1, the streamwise vorticity ω_1 and the rotation-induced pressure p_R are shown in panels (*a–d*), respectively. As shown in figure 15(*a*), the vortices are almost streamwise, while no typical hairpin vortex is found. In addition, the comparison of the four panels shows that in contrast to h, the other three quantities, including h_1, exhibit stronger correlations with the vortices filtered by the Q criterion. It could mainly be attributed to two reasons. On one hand, the vortices are predominantly aligned in the streamwise direction. Therefore, the streamwise components h_1 and ω_1, along with the streamwise rotation-induced pressure p_R, are expected to exhibit a stronger coherence with these vortices. On the other hand, vorticity and vortex are different, especially in viscous flows with strong shear (Moin, Leonard & Kim 1986; Charkrit, Shrestha & Liu 2020). Given that the helicity is defined based on the local relationship between vorticity and velocity, it follows naturally that the overall helicity is not well distributed on the surface of the vortices. In fact, the helicity can better reflect the vortex dynamics in the log-law layer. Additionally, in near-wall dynamics under the buffer layer, as discussed earlier, helicity still elucidates some crucial processes from the perspectives of chirality and could be correlated with the streaks, which will be further explored in the following discussion.

To quantitatively identify the rotation effects on the vortices, two angles are used in the following analysis. In the buffer layer where turbulence is generated by strain, the streaks rise to form the streamwise vortices. Therefore, the lift angles of the streak are considered here. The streaks are first extracted through the condition $u_1^+ < 0$, and then the lift angle θ_l for every streak is evaluated as (Schoppa & Hussain 2002)

$$\theta_l = \tan^{-1}\left|\frac{\partial u_1/\partial x_3}{\mathrm{d}\langle U_1\rangle/\mathrm{d}x_2}\right|_{\max}. \tag{4.1}$$

Figure 16(*a*) shows the fluctuating velocity u_1^+ on the slice $x_2^+ = 20.0$, with the blue contour depicting the distribution of streaks. The streaks extracted by $u_1^+ < -2$ are displayed in figure 16(*b*), together with the contour of δh with $r_1^+ = 47.1$. As shown, δh is primarily concentrated in the vicinity of the streaks, indicating a strong relationship

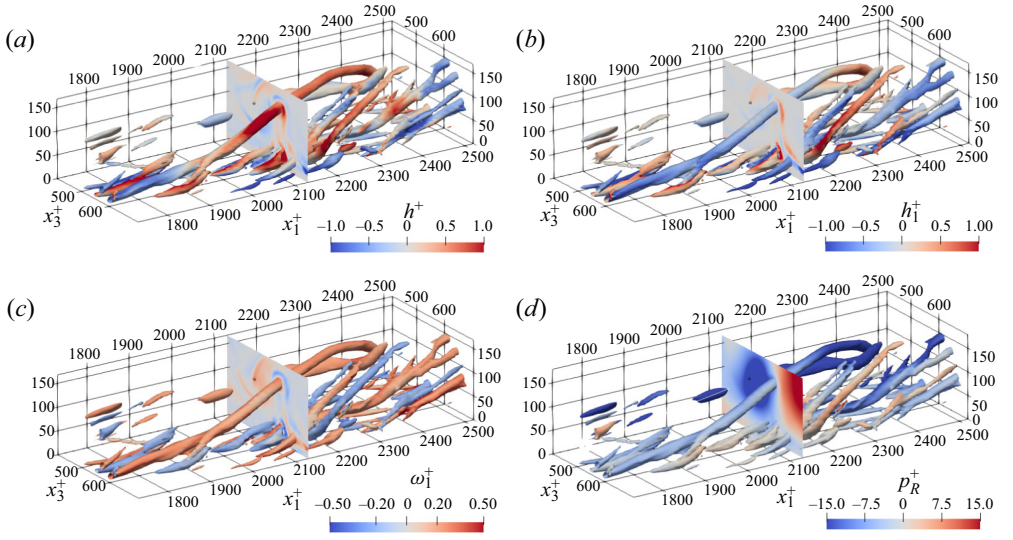

Figure 15. Distribution of quantities on typical vortices in ST30 drawn with $Q > 400$. The slices show the distribution of the quantities at $x_1^+ = 2147.4$. (*a*) Fluctuating helicity h^+. (*b*) Streamwise fluctuating helicity h_1^+. (*c*) Streamwise fluctuating vorticity ω_1^+. (*d*) Rotation-induced pressure p_R^+.

between the streaks and δh within this layer. The lift angle θ_l is then compared with the cross-section of two streaks in figure 16(*c*). As x_2^+ increases, the streaks gradually roll up to form streamwise vortices in the rotating channel and the lift angles increase from zero towards higher values. The angles 33° and 72° marked in this figure are the peak values of the probability density function (p.d.f.) of θ_l in ST30 at $x_2^+ = 10.5$ and 20.0, respectively. The p.d.f. of θ_l is shown in figures 16(*c*) and 16(*d*), where panel (*c*) gives the p.d.f. at $x_2^+ = 10.5$ and panel (*d*) gives the p.d.f. at $x_2^+ = 20.0$. The rotation effects are more apparent at $x_2^+ = 10.5$. As rotation intensifies, the lift angle distributes in a wider range. Generally, rotation enhances the extraction of energy and helicity from the mean fields. As Re_τ increases, the rotation effects diminish, consistent with the earlier discussions.

In non-rotating channel turbulence, one of the main flow structures is the hairpin vortex, which rises from the streaks in the buffer layer. Within the log-law layer, the hairpin vortex sweeps down and then breaks into various small-scale structures. The instability of the spanwise component of the hairpin vortex plays important roles in the sweep events (Jiménez & Pinelli 1999; Adrian 2007). To quantitatively evaluate the rotation effects on the spanwise vortices in the log-law layer, an angle can be defined through the vorticity:

$$\theta_\omega = \tan^{-1} |\omega_3/\omega_1|_{Q>50}\,. \tag{4.2}$$

When $\theta_\omega = 0°$, the vortex is fully streamwise, whereas when $\theta_\omega = 90°$, the vortex is fully spanwise. The condition of $Q > 50$ is used to get more stable statistics and gives the same qualitative conclusions with $Q > 400$. Figure 17(*a*,*b*) compares the vortices of ST07 and ST30 in the log-law layer. As shown, the vortices of ST07 are almost streamwise under $x_2^+ < 110$ but spanwise at higher layers. In comparison, the vortices of ST30 are almost streamwise with a slightly tilted angle. As shown in figure 17(*c*), ST00 and ST07 have similar p.d.f. distributions. However, as rotation intensifies, the streamwise vortices are strengthened and the spanwise vortices almost diminish when $Ro_\tau = 60$. The suppression of the spanwise vortices by rotation reduces the frequency of sweep events and constrains

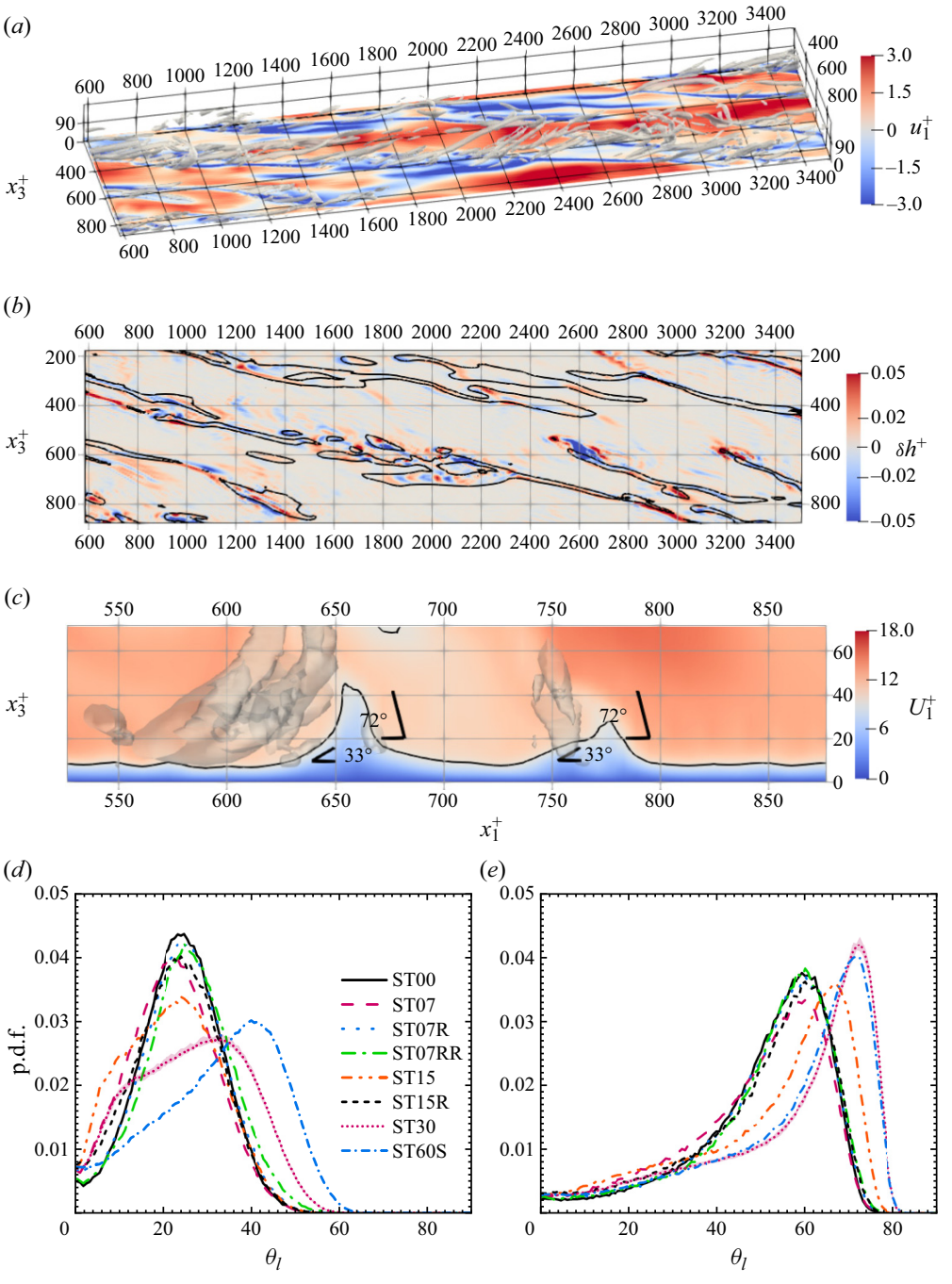

Figure 16. Streaks and their lift angles of ST30. (*a*) Contour of u_1^+ at $x_2^+ = 20.0$. The grey transparent structures are obtained using the Q criterion $Q > 400$. (*b*) Distribution of δh^+ at $x_2^+ = 20.0$ with $r_1^+ = 47.1$. The black solid lines are the isolines of $u_1^+ = -2$. (*c*) Contour of U_1^+ at $x_1^+ = 2757.6$. The black solid line shows the isoline of $U_1^+ = 9.0$. (*d*,*e*) P.d.f. of the streak lift angles θ_l at $x_2^+ = 10.5$ and $x_2^+ = 20.0$, respectively. The pink filled region in panel (*e*,*f*) shows the error bars of the p.d.f. of ST30.

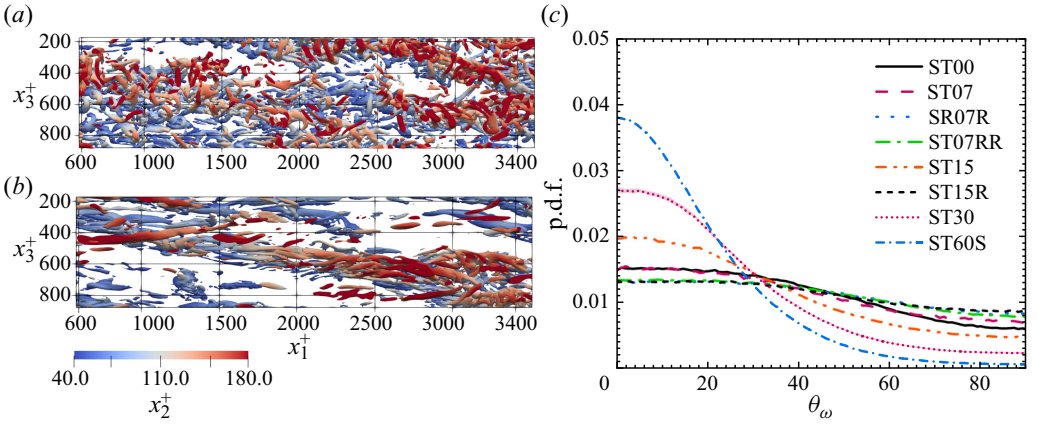

Figure 17. Vortices in the log-law layer and the p.d.f. of the vortex angle θ_ω. (*a*,*b*) Vortices in the log-law layer ($x_2^+ \in [40.0, 180.0]$) coloured by x_2^+ with $Q > 50$ of ST07 and ST30, respectively. (*c*) P.d.f of vortex angles θ_ω at $x_2^+ = 80.0$ and the pink filled region shows the error bar of the p.d.f. of ST30.

the energy cascades towards small scales (Hu *et al.* 2023). It thus strengthens the TKE in the log-law layer, especially $\langle u_2^2 \rangle$ and $\langle u_3^2 \rangle$ related to the streamwise vorticity ω_1, consistent with the Reynolds stress budget discussed by Yang & Wang (2018). In contrast, as Re_τ increases, the vortex angles strongly decrease. The opposing effects of Re_τ and Ro_τ are consistent with the DHGKE results (figure 13).

5. Conclusions

Channel turbulence with streamwise rotation is a typical case of helicity in conjunction with boundary effects. As another inviscid invariant in addition to energy, helicity is a quantitative representation of vortex topology. In this paper, we have investigated the detail of helicity and vortex structures in streamwise-rotating channel turbulence.

First, we give the basic statistics about helicity. The mean helicity and fluctuating helicity are both positive under the buffer layer but negative in the log-law layer. The streamwise component is nearly antisymmetry with the spanwise component in the viscous sublayer, which is the near-wall behaviour of these helicity components. As Re_τ/Ro_τ decreases, the peak of the fluctuating helicity shifts towards the wall. This suggests the rotation effects could penetrate deeper regions within the boundary layer and have potential impacts in accelerating the turbulent transition. Second, for the helicity budget, we find that the pressure term transfers positive helicity from the channel centre towards the wall and is the main source of the helicity. The Coriolis force and the production mainly restrain the helicity. The opposing effects of Re_τ and Ro_τ can be related to the competitive mechanisms between turbulent convections and rotation effects (Coriolis term and corresponding pressure term). Then, the near-wall behaviours of the helicity budget are derived and verified.

The multiscale behaviours of the helicity are then discussed using the differentiated generalized Kolmogorov equation. Through the scale helicity distribution, we find that the sign change of the scale helicity first happens at small scales and then expands to large scales. Especially, in the buffer layer, the scale helicity is negative at small scales but positive at large scales. Different from the energy, helicity is directly affected by the Coriolis effects and the pressure transfers. As rotation intensifies, the two effects become

more important. In the buffer layer, the production and the spatial turbulent convection reach their extremes at small scales, aligning with the distribution of the scale helicity. This suggests a strong relationship between the two terms and the sign change of the scale helicity. The interscale turbulent convection cascades scale helicity among scales, and diminish the negative helicity at small scales and the positive helicity at large scales at the same time. Then, the main effects around the helicity peaks are evaluated. It is confirmed that the interscale turbulent convection is strongly affected by Re_τ, while other key terms are mainly affected by Ro_τ. In the log-law layer, different from the terms in scale energy balance, the spatial transfers induced by rotation play important roles in budget for the scale helicity. Then, the correlation analysis is performed for the DHGKE budget. The large-scale sweep effects (Baj *et al.* 2022) and other basic results are confirmed. Additionally, the relations between the spatial and interscale effects are found and explained by the expansions in two-point correlation.

To investigate the physical meaning of the helicity, we study the vortex structures based on the Q criterion. We find that helicity is not well distributed on the surface of vortices. It is due to the discrepancy between vorticity and vortex induced by strong shear stresses. However, helicity could still illustrate some key processes from the perspectives of chirality and be related to streaks. As rotation intensifies or the Reynolds numbers decreases, the streak lift angles have wider ranges, indicating stronger turbulence generation. It is consistent with the tendencies of the peak laws under the buffer layer. In the log-law layer, in non-rotating channel turbulence, the spanwise vortices are closely related to the sweep events and the interscale cascades. Rotation suppresses the spanwise vortices in the log-law layer and thus inhibits the breaking of coherent structures and the forward cascades. The opposing effects of Re_τ and Ro_τ are also found here, and could be linked to the competitive effects of the turbulent convections and rotation effects.

In this paper, we discuss the spatial and interscale dynamics in streamwise-rotating channel turbulence. The opposing effects of Re_τ and Ro_τ, the interscale dynamics of the scale helicity, and the relation between the helicity and vortices are investigated in detail. Helicity in fact plays as an important quantity in the turbulent channel flow with streamwise rotation. In the future, helicity is expected to be investigated in more asymmetrical turbulent flows and applied for further turbulent modelling.

Funding. This work was supported by the National Key Research and Development Program of China (grant nos. 2020YFA0711800 and 2019YFA0405300) and NSFC Projects (grant nos. 12072349, 12232018, 91852203 and 12202457).

Declaration of interests. The authors report no conflict of interest.

Author ORCIDs.
Running Hu https://orcid.org/0000-0002-3423-5583;
Changping Yu https://orcid.org/0000-0002-2126-1344.

Appendix A. Basic statistics and error estimations

A.1. *Basic statistics*

Figure 18(*a*,*b*) shows the profiles of mean velocities $\langle U_1^+ \rangle$ and $\langle U_3^+ \rangle$, respectively. With increasing rotation rates, $\langle U_1^+ \rangle$ is suppressed, while $\langle U_3^+ \rangle$ is enhanced. As Re_τ intensifies, $\langle U_1^+ \rangle$ and $\langle U_3^+ \rangle$ both slightly increase. Figure 19(*a*,*b*) shows the profiles of mean vorticities $\langle W_1^+ \rangle$ and $\langle W_3^+ \rangle$, respectively. The amplitudes of $\langle W_1^+ \rangle$ are increased by rotation but not affected by Re_τ. In contrast, $\langle W_3^+ \rangle$ only slightly affected by strong rotation $Ro_\tau > 30$.

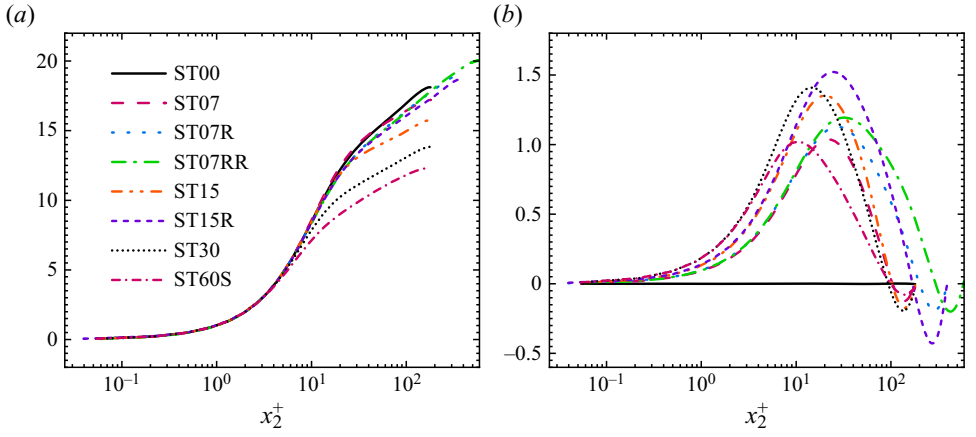

Figure 18. Profile of mean velocity: (*a*) $\langle U_1 \rangle^+$; (*b*) $\langle U_3 \rangle^+$.

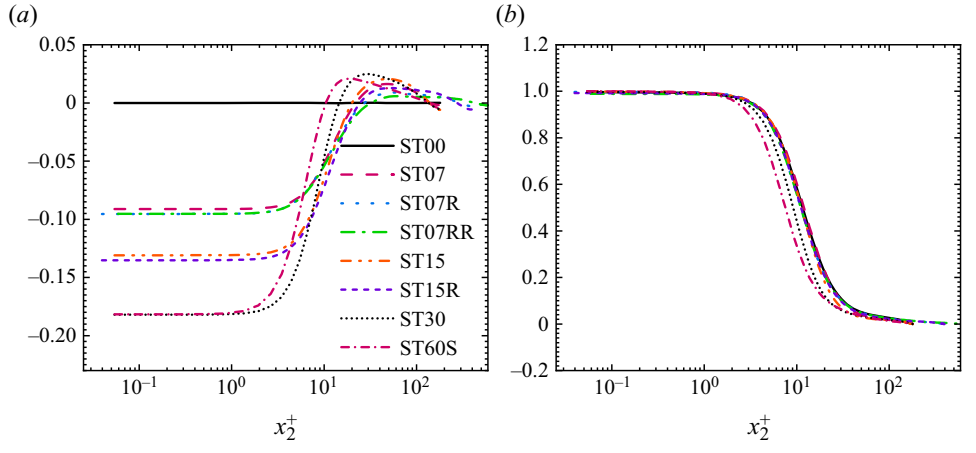

Figure 19. Profile of mean vorticity: (*a*) $\langle W_1 \rangle^+$; (*b*) $\langle W_3 \rangle^+$.

A.2. *Error estimations*

To estimate the error of the main statistics, the error bars are introduced by calculating the standard deviation (S.D.). For any dataset $\{x_i\}$, S.D. is defined as

$$S.D. = \sqrt{\frac{1}{n-1}\sum (x_i - \bar{x})^2}, \tag{A1}$$

where $\bar{x}$ is the mean value of the dataset $\{x_i\}$ and n is the number of the data in the dataset.

Figure 20 gives error bar details of the mean helicity H^+ shown in figure 1(*b*). The error is indistinguishable compared with the mean value. Similar error bars have been shown for the fluctuating helicity (figure 2*b*), scale helicity (figure 7*a*), scale pressure (figure 8), streak lift angles (figure 16*d*,*e*) and vortex angles (figure 17*c*).

The error bars of the fluctuating helicity budget and DHGKE are not shown in the main contents, and the quality of the dataset can partially be verified by the balance of the budget (the term '*sum*'). For completeness, the error bar of the poorest quality statistics (DHGKE balance in the log-law layer in figure 12) are given in figure 21. Specifically,

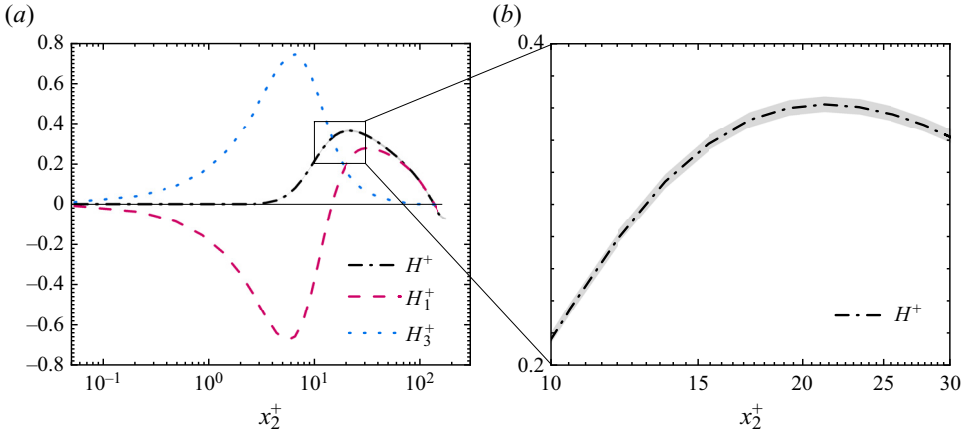

Figure 20. (*a*) Decomposed helicity H_i^+ of ST30 and the grey filled region shows the error bar of H^+. (*b*) Details about the error bars.

we show the error bar of the terms *sum* and T^{SS+} in the log-law layer of (*a*) ST07 with 81 slices, (*b*) ST30 with 41 slices, (*c*) ST07 with 41 slices and (*d*) ST07 of only one time slice. The results of ST30 in figure 21(*b*) are of high quality, even with only 41 time slices. In contrast, the results of ST07 in figure 21(*a*) have apparently wider error bars, even with 81 time slices. This difference may be attributed to the fact that in the log-law layer, the helicity distribution in ST30 is stronger than that in ST07. The comparison between figures 21(*a*) and 21(*c*) shows the effects of the time slice numbers on the error bar. The width of the error bar is almost unaffected by the time slice numbers. However, compared with the results with 81 slices (figure 21*a*), if only 41 slices (figure 21*c*) are used, the mean values of the term *sum* deviate more apparently from zero. It can be inferred that 161 slices of data will not have an apparent influence on the error bar. In fact, for a sufficiently large dataset, the S.D. is independent of the data size. For example, the S.D. of evenly distributed random numbers between 0 and 1 is $1/2\sqrt{3}$ and is independent of the data size. Figure 21(*d*) shows the result of only one time slice. It has larger variances, which directly affect the error bars in figures 21(*a*) and 21(*c*).

Appendix B. Near-wall behaviours of the helicity budget

According to the symmetry, the fluctuating velocities in the vicinity of the wall are estimated as (Kim, Moin & Moser 1987)

$$\left.\begin{aligned} u_1 \sim x_2, \quad u_2 \sim x_2^2, \quad u_3 \sim x_2, \\ \omega_1 \sim 1, \quad \omega_2 \sim x_2, \quad \omega_3 \sim 1. \end{aligned}\right\} \tag{B1}$$

The mean velocity can be estimated as

$$\left.\begin{aligned} \langle U_1 \rangle \sim x_2, \quad \langle U_2 \rangle = 0, \quad \langle U_3 \rangle \sim x_2, \\ \langle W_1 \rangle \sim 1, \quad \langle W_2 \rangle \sim x_2, \quad \langle W_3 \rangle \sim 1. \end{aligned}\right\} \tag{B2}$$

B.1. *The balance in the vicinity of the wall*

We then expand the helicity budget based on these relations.

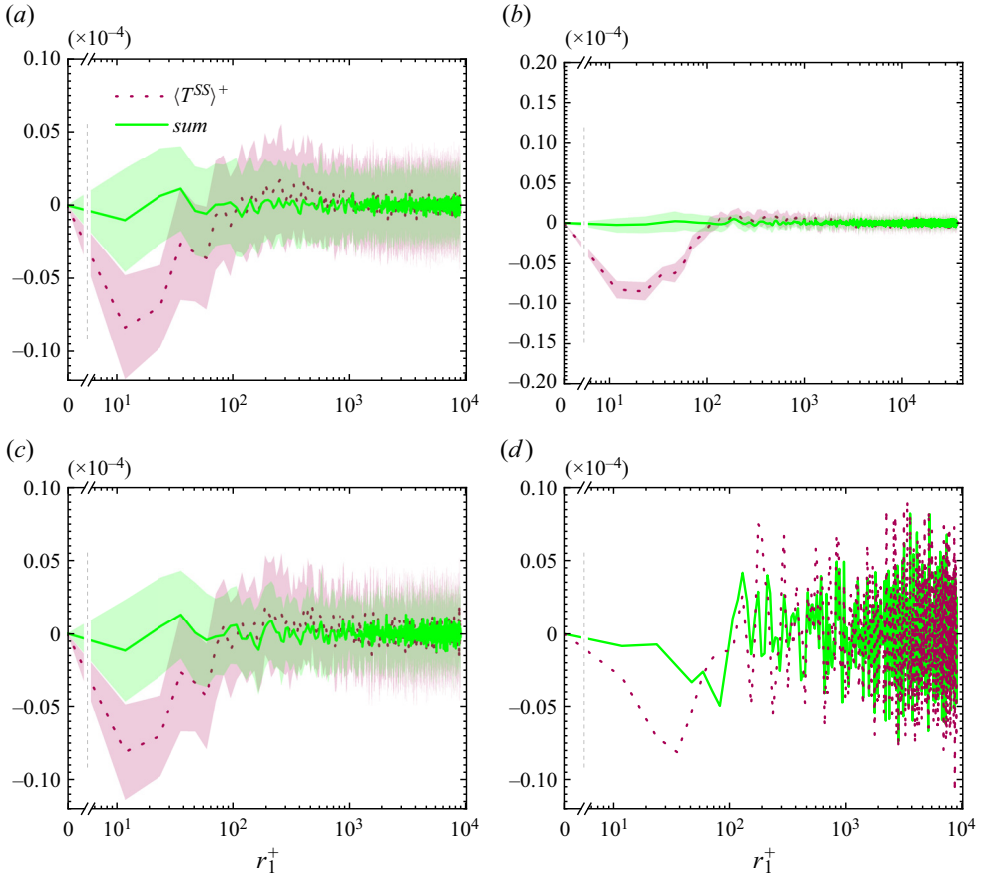

Figure 21. Error bars of DHGKE in the log-law layer of (*a*) ST07 with 81 slices, (*b*) ST30 with 41 slices, (*c*) ST07 with 41 slices and (*d*) ST07 of only one time slice.

The production is

$$\begin{aligned}\langle \Pi \rangle &= -\frac{\mathrm{d}\langle u_2u_3\rangle}{\mathrm{d}x_2}\frac{\mathrm{d}\langle U_1\rangle}{\mathrm{d}x_2} + \frac{\mathrm{d}\langle u_1u_2\rangle}{\mathrm{d}x_2}\frac{\mathrm{d}\langle U_3\rangle}{\mathrm{d}x_2} - \langle u_iu_2\rangle\frac{\mathrm{d}\langle W_i\rangle}{\mathrm{d}x_2} \\ &\sim -\frac{\mathrm{d}\langle u_2u_3\rangle}{\mathrm{d}x_2}\frac{\mathrm{d}\langle U_1\rangle}{\mathrm{d}x_2} + \frac{\mathrm{d}\langle u_1u_2\rangle}{\mathrm{d}x_2}\frac{\mathrm{d}\langle U_3\rangle}{\mathrm{d}x_2} \\ &\sim x_2^2. \end{aligned} \tag{B3}$$

The turbulent convection is

$$\begin{aligned}\langle T \rangle &= \frac{\mathrm{d}\langle hu_2\rangle}{\mathrm{d}x_2} - \frac{1}{2}\frac{\mathrm{d}}{\mathrm{d}x_2}\langle u_iu_i\omega_2\rangle \\ &\sim \frac{\mathrm{d}}{\mathrm{d}x_2}\langle (u_1\omega_1 + u_3\omega_3)u_2\rangle - \frac{1}{2}\frac{\mathrm{d}}{\mathrm{d}x_2}\langle (u_1u_1 + u_3u_3)\omega_2\rangle \\ &\sim x_2^2. \end{aligned} \tag{B4}$$

The Coriolis term is

$$C = 2\frac{\mathrm{d}\langle u_1u_2\rangle}{\mathrm{d}x_2}\Omega \sim x_2^2. \tag{B5}$$

The viscous diffusion is

$$D = \nu \frac{\mathrm{d}^2 \langle h \rangle}{\mathrm{d}x_2^2} \sim \nu \frac{\mathrm{d}^2}{\mathrm{d}x_2^2} \langle u_1\omega_1 + u_3\omega_3 \rangle \sim 1. \tag{B6}$$

The pseudo-dissipation is

$$\begin{aligned} -E &= -2\nu \left\langle \frac{\partial u_i}{\partial x_j} \frac{\partial \omega_i}{\partial x_j} \right\rangle \\ &\sim -2\nu \left\langle \frac{\partial u_1}{\partial x_2} \frac{\partial \omega_1}{\partial x_2} + \frac{\partial u_3}{\partial x_2} \frac{\partial \omega_3}{\partial x_2} \right\rangle \sim 1. \end{aligned} \tag{B7}$$

The pressure transport is

$$G = -\frac{1}{\rho} \frac{\mathrm{d} \langle \omega_2 p \rangle}{\mathrm{d}x_2} \sim -\frac{1}{\rho} \left\langle p \frac{\partial \omega_2}{\partial x_2} \right\rangle \sim 1, \tag{B8}$$

where we use that $p \sim 1$, because the root-mean-square of pressure on the wall is non-zero (Yang *et al.* 2018).

B.2. *The balance on the wall*

The viscous diffusion on the wall is

$$\begin{aligned} D|_{x_2=\pm h} &= \nu \frac{\mathrm{d}^2 \langle h \rangle}{\mathrm{d}x_2^2}\bigg|_{x_2=\pm h} = \nu \frac{\mathrm{d}^2}{\mathrm{d}x_2^2} \langle u_1\omega_1 + u_2\omega_2 + u_3\omega_3 \rangle \bigg|_{x_2=\pm h} \\ &= \nu \frac{\mathrm{d}^2}{\mathrm{d}x_2^2} \langle u_1\omega_1 + u_3\omega_3 \rangle \bigg|_{x_2=\pm h} \\ &= \nu \frac{\mathrm{d}^2}{\mathrm{d}x_2^2} \left\langle u_1 \left(\frac{\partial u_3}{\partial x_2} - \frac{\partial u_2}{\partial x_3} \right) + u_3 \left(\frac{\partial u_2}{\partial x_1} - \frac{\partial u_1}{\partial x_2} \right) \right\rangle \bigg|_{x_2=\pm h} \\ &= \nu \frac{\mathrm{d}^2}{\mathrm{d}x_2^2} \left\langle u_1 \frac{\partial u_3}{\partial x_2} - u_3 \frac{\partial u_1}{\partial x_2} \right\rangle \bigg|_{x_2=\pm h} \\ &= \nu \left\langle \left(\frac{\partial^2 u_1}{\partial x_2^2} \frac{\partial u_3}{\partial x_2} + \frac{\partial u_1}{\partial x_2} \frac{\partial^2 u_3}{\partial x_2^2} + \frac{\partial u_1}{\partial x_2} \frac{\partial^2 u_3}{\partial x_2^2} + u_1 \frac{\partial^3 u_3}{\partial x_2^3} \right) \right. \\ &\quad \left. - \left(\frac{\partial u_1}{\partial x_2} \frac{\partial^2 u_3}{\partial^2 x_2} + \frac{\partial^2 u_1}{\partial x_2^2} \frac{\partial u_3}{\partial x_2} + \frac{\partial^2 u_1}{\partial x_2^2} \frac{\partial u_3}{\partial x_2} + \frac{\partial^3 u_1}{\partial x_2^3} u_3 \right) \right\rangle \bigg|_{x_2=\pm h} \\ &= \nu \left\langle \frac{\partial u_1}{\partial x_2} \frac{\partial^2 u_3}{\partial x_2^2} - \frac{\partial^2 u_1}{\partial x_2^2} \frac{\partial u_3}{\partial x_2} \right\rangle \bigg|_{x_2=\pm h}, \end{aligned} \tag{B9}$$

where

$$\frac{\partial^2}{\partial x_2^2}\left(u_1\frac{\partial u_3}{\partial x_2}\right)=\frac{\partial}{\partial x_2}\left(\frac{\partial u_1}{\partial x_2}\frac{\partial u_3}{\partial x_2}+u_1\frac{\partial^2 u_3}{\partial x_2^2}\right)$$
$$=\frac{\partial^2 u_1}{\partial x_2^2}\frac{\partial u_3}{\partial x_2}+\frac{\partial u_1}{\partial x_2}\frac{\partial^2 u_3}{\partial x_2^2}+\frac{\partial u_1}{\partial x_2}\frac{\partial^2 u_3}{\partial x_2^2}+u_1\frac{\partial^3 u_3}{\partial x_2^3} \tag{B10}$$

and

$$\frac{\partial^2}{\partial x_2^2}\left(u_3\frac{\partial u_1}{\partial x_2}\right)=\frac{\partial}{\partial x_2}\left(\frac{\partial u_3}{\partial x_2}\frac{\partial u_1}{\partial x_2}+u_3\frac{\partial^2 u_1}{\partial x_2^2}\right)$$
$$=\frac{\partial^2 u_3}{\partial^2 x_2}\frac{\partial u_1}{\partial x_2}+\frac{\partial u_3}{\partial x_2}\frac{\partial^2 u_1}{\partial x_2^2}+\frac{\partial u_3}{\partial x_2}\frac{\partial^2 u_1}{\partial x_2^2}+u_3\frac{\partial^3 u_1}{\partial x_2^3}. \tag{B11}$$

The pseudo-dissipation on the wall is

$$-E|_{x_2=\pm h}=-2\nu\left\langle\frac{\partial u_i}{\partial x_j}\frac{\partial \omega_i}{\partial x_j}\right\rangle\Big|_{x_2=\pm h}=-2\nu\left\langle\frac{\partial u_i}{\partial x_2}\frac{\partial \omega_i}{\partial x_2}\right\rangle\Big|_{x_2=\pm h}$$
$$=-2\nu\left\langle\frac{\partial u_1}{\partial x_2}\left(\frac{\partial^2 u_3}{\partial x_2^2}-\frac{\partial^2 u_2}{\partial x_2\partial x_3}\right)+\frac{\partial u_3}{\partial x_2}\left(\frac{\partial^2 u_2}{\partial x_1\partial x_2}-\frac{\partial^2 u_1}{\partial x_2^2}\right)\right\rangle\Big|_{x_2=\pm h}$$
$$=-2\nu\left\langle\frac{\partial u_1}{\partial x_2}\frac{\partial^2 u_3}{\partial x_2^2}-\frac{\partial u_3}{\partial x_2}\frac{\partial^2 u_1}{\partial x_2^2}\right\rangle\Big|_{x_2=\pm h}. \tag{B12}$$

Except for the pressure term and the viscous effects, all other terms are zeros on the wall. Therefore,

$$G|_{x_2=\pm h}=D|_{x_2=\pm h}=\tfrac{1}{2}E|_{x_2=\pm h}. \tag{B13}$$

Appendix C. Expansion by two-point correlations of turbulent convection and viscous diffusion

The interscale turbulent helicity transfer:

$$T^{H,SS}=-\frac{\partial}{\partial r_1}\frac{\partial}{\partial r_j}\left(\delta h\delta u_j\right)+\frac{\partial}{\partial r_1}\frac{1}{2}\frac{\partial}{\partial r_j}\left(\delta\omega_j\delta u^2\right)$$
$$=\frac{1}{2}\frac{\partial}{\partial r_1}\left[\frac{\partial}{\partial x_j}\left(-u_i\omega_i u_j+\frac{1}{2}u_i u_i\omega_j\right)+\omega_i'\frac{\partial}{\partial x_j}u_i u_j+u_i'\frac{\partial}{\partial x_j}(\omega_i u_j-u_i\omega_j)\right.$$
$$+u_j'\frac{\partial}{\partial x_j}u_i\omega_i-\frac{1}{2}\omega_j'\frac{\partial}{\partial x_j}u_i u_i-u_i'u_j'\frac{\partial}{\partial x_j}\omega_i-u_i'\omega_i'\frac{\partial}{\partial x_j}u_j$$
$$\left.+(u_i'\omega_j'-\omega_i'u_j')\frac{\partial}{\partial x_j}u_i+\frac{1}{2}u_i'u_i'\frac{\partial}{\partial x_j}\omega_j+S.P.\right], \tag{C1}$$

where $S.P.$ represents the symmetry part. For instance, $S.P.$ of $-\langle\omega_i'u_j'\partial u_i/\partial x_j\rangle$ is $-\langle\omega_i u_j\partial u_i'/\partial x_j'\rangle$.

The spatial turbulent helicity transfer:

$$\begin{aligned} T^{H,SP} &= \frac{\partial}{\partial r_1}\left[-\frac{\partial}{\partial X_j}\left(u_j^*\delta h\right)+\frac{1}{2}\frac{\partial}{\partial X_j}\left(\delta u^2\omega_j^*\right)\right] \\ &= \frac{1}{2}\frac{\partial}{\partial r_1}\left[\frac{\partial}{\partial x_j}\left(-u_i\omega_i u_j+\frac{1}{2}u_i u_i\omega_j\right)+\omega_i'\frac{\partial}{\partial x_j}u_i u_j+u_i'\frac{\partial}{\partial x_j}(\omega_i u_j-u_i\omega_j)\right. \\ &\quad -u_j'\frac{\partial}{\partial x_j}u_i\omega_i+\frac{1}{2}\omega_j'\frac{\partial}{\partial x_j}u_i u_i+u_i'u_j'\frac{\partial}{\partial x_j}\omega_i-u_i'\omega_i'\frac{\partial}{\partial x_j}u_j \\ &\quad \left.-(u_i'\omega_j'-\omega_i'u_j')\frac{\partial}{\partial x_j}u_i+\frac{1}{2}u_i'u_i'\frac{\partial}{\partial x_j}\omega_j+S.P.\right]. \end{aligned} \tag{C2}$$

The interscale viscous diffusion:

$$\begin{aligned} D^{SS} &= 2\nu\frac{\partial}{\partial r_1}\frac{\partial^2\delta h}{\partial r_j\partial r_j} \\ &= \frac{\nu}{2}\frac{\partial}{\partial r_1}\left[\frac{\partial^2 u_i\omega_i}{\partial x_j\partial x_j}-\omega_i'\frac{\partial^2 u_i}{\partial x_j\partial x_j}-u_i'\frac{\partial^2\omega_i}{\partial x_j\partial x_j}+2\frac{\partial u_i}{\partial x_j}\frac{\partial\omega_i'}{\partial x_j'}+S.P.\right]. \end{aligned} \tag{C3}$$

The spatial viscous diffusion:

$$\begin{aligned} D^{SP} &= \frac{\nu}{2}\frac{\partial}{\partial r_1}\frac{\partial^2\delta h}{\partial X_j\partial X_j} \\ &= \frac{\nu}{2}\frac{\partial}{\partial r_1}\left[\frac{\partial^2 u_i\omega_i}{\partial x_j\partial x_j}-\omega_i'\frac{\partial^2 u_i}{\partial x_j\partial x_j}-u_i'\frac{\partial^2\omega_i}{\partial x_j\partial x_j}-2\frac{\partial u_i}{\partial x_j}\frac{\partial\omega_i'}{\partial x_j'}+S.P.\right]. \end{aligned} \tag{C4}$$

References

Adrian, R.J. 2007 Hairpin vortex organization in wall turbulence. *Phys. Fluids* **19** (4), 041301.

Alexakis, A. & Biferale, L. 2018 Cascades and transitions in turbulent flows. *Phys. Rep.* **767–769**, 1–101.

Baj, P., Portela, F.A. & Carter, D.W. 2022 On the simultaneous cascades of energy, helicity, and enstrophy in incompressible homogeneous turbulence. *J. Fluid Mech.* **952**, A20.

Biferale, L., Boffetta, G., Celani, A., Lanotte, A., Toschi, F. & Vergassola, M. 2003 The decay of homogeneous anisotropic turbulence. *Phys. Fluids* **15** (8), 2105–2112.

Brissaud, A., Frisch, U., Leorat, J., Lesieur, M. & Mazure, A. 1973 Helicity cascades in fully developed isotropic turbulence. *Phys. Fluids* **16** (8), 1366–1367.

Charkrit, S., Shrestha, P. & Liu, C. 2020 Liutex core line and POD analysis on hairpin vortex formation in natural flow transition. *J. Hydrodyn.* **32** (6), 1109–1121.

Chen, Q., Chen, S. & Eyink, G.L. 2003*a* The joint cascade of energy and helicity in three-dimensional turbulence. *Phys. Fluids* **15** (2), 361–374.

Chen, Q., Chen, S., Eyink, G.L. & Holm, D.D. 2003*b* Intermittency in the joint cascade of energy and helicity. *Phys. Rev. Lett.* **90** (21), 214503.

Cimarelli, A., De Angelis, E. & Casciola, C.M. 2013 Paths of energy in turbulent channel flows. *J. Fluid Mech.* **715**, 436–451.

Cimarelli, A., De Angelis, E., Jimenez, J. & Casciola, C.M. 2016 Cascades and wall-normal fluxes in turbulent channel flows. *J. Fluid Mech.* **796**, 417–436.

Cimarelli, A., De Angelis, E., Schlatter, P., Brethouwer, G., Talamelli, A. & Casciola, C.M. 2015 Sources and fluxes of scale energy in the overlap layer of wall turbulence. *J. Fluid Mech.* **771**, 407–423.

Dai, Y.-J., Huang, W.-X. & Xu, C.-X. 2016 Effects of Taylor–Görtler vortices on turbulent flows in a spanwise-rotating channel. *Phys. Fluids* **28** (11), 115104.

DAI, Y.-J., HUANG, W.-X. & XU, C.-X. 2019 Coherent structures in streamwise rotating channel flow. *Phys. Fluids* **31** (2), 021204.

DANAILA, L., ANSELMET, F., ZHOU, T. & ANTONIA, R.A. 2001 Turbulent energy scale budget equations in a fully developed channel flow. *J. Fluid Mech.* **430**, 87–109.

DAVIDSON, P.A. 2013 *Turbulence in Rotating, Stratified and Electrically Conducting Fluids*. Cambridge University Press.

DAVIDSON, P.A. 2015 *Turbulence: An Introduction for Scientists and Engineers*. Oxford University Press.

DAVIDSON, P.A. 2016 *Introduction to Magnetohydrodynamics*, 2nd edn. Cambridge University Press.

GATTI, D., CHIARINI, A., CIMARELLI, A. & QUADRIO, M. 2020 Structure function tensor equations in inhomogeneous turbulence. *J. Fluid Mech.* **898**, A5.

HIEJIMA, T. 2020 Helicity effects on inviscid instability in Batchelor vortices. *J. Fluid Mech.* **897**, A37.

HU, R., LI, X. & YU, C. 2022*a* Effects of the Coriolis force in inhomogeneous rotating turbulence. *Phys. Fluids* **34** (3), 035108.

HU, R., LI, X. & YU, C. 2022*b* Transfers of energy and helicity in helical rotating turbulence. *J. Fluid Mech.* **946**, A19.

HU, R., LI, X. & YU, C. 2023 Multiscale dynamics in streamwise-rotating channel turbulence. *J. Fluid. Mech.* **972**, A14.

IRVINE, W.T.M. 2018 Moreau's hydrodynamic helicity and the life of vortex knots and links. *Comptes Rendus Mécanique*, **346** (3), 170–174.

JIMÉNEZ, J. & PINELLI, A. 1999 The autonomous cycle of near-wall turbulence. *J. Fluid Mech.* **389**, 335–359.

JING, Z. & DUCOIN, A. 2020 Direct numerical simulation and stability analysis of the transitional boundary layer on a marine propeller blade. *Phys. Fluids* **32** (12), 124102.

JOHNSTON, J.P., HALLEENT, R.M. & LEZIUS, D.K. 1972 Effects of spanwise rotation on the structure of two-dimensional fully developed turbulent channel flow. *J. Fluid Mech.* **56** (3), 533.

KIM, J. 1989 On the structure of pressure fluctuations in simulated turbulent channel flow. *J. Fluid Mech.* **205**, 421–451.

KIM, J., MOIN, P. & MOSER, R. 1987 Turbulence statistics in fully developed channel flow at low Reynolds number. *J. Fluid Mech.* **177**, 133–166.

KOLMOGOROV, A.N. 1941 The local structure of turbulence in incompressible viscous fluid for very large Reynolds numbers. *C. R. Acad. Sci. URSS* **30**, 301–305.

KRISTOFFERSEN, R. & ANDERSSON, H.I. 1993 Direct simulations of low-Reynolds-number turbulent flow in a rotating channel. *J. Fluid Mech.* **256**, 163–197.

LIU, Y., TANG, Y., SCILLITOE, A.D. & TUCKER, P.G. 2020 Modification of shear stress transport turbulence model using helicity for predicting corner separation flow in a linear compressor cascade. *Trans. ASME J. Turbomach.* **142** (2), 021004.

MARATI, N., CASCIOLA, C.M. & PIVA, R. 2004 Energy cascade and spatial fluxes in wall turbulence. *J. Fluid Mech.* **521**, 191–215.

MARUSIC, I. & MONTY, J.P. 2019 Attached eddy model of wall turbulence. *Annu. Rev. Fluid Mech.* **51**, 49–74.

MASUDA, S., FUKUDA, S. & NAGATA, M. 2008 Instabilities of plane Poiseuille flow with a streamwise system rotation. *J. Fluid Mech.* **603**, 189–206.

MININNI, P.D. & POUQUET, A. 2009 Helicity cascades in rotating turbulence. *Phys. Rev.* E **79** (2), 026304.

MININNI, P.D. & POUQUET, A. 2010 Rotating helical turbulence. I. Global evolution and spectral behavior. *Phys. Fluids* **22** (3), 035105.

MININNI, P.D., ROSENBERG, D. & POUQUET, A. 2012 Isotropization at small scales of rotating helically driven turbulence. *J. Fluid Mech.* **699**, 263–279.

MOFFATT, H.K. & TSINOBER, A. 1992 Helicity in laminar and turbulent flow. *Annu. Rev. Fluid Mech.* **24** (1), 281–312.

MOIN, P., LEONARD, A. & KIM, J. 1986 Evolution of a curved vortex filament into a vortex ring. *Phys. Fluids* **29** (4), 955–963.

MOLLICONE, J.P., BATTISTA, F., GUALTIERI, P. & CASCIOLA, C.M. 2018 Turbulence dynamics in separated flows: the generalised Kolmogorov equation for inhomogeneous anisotropic conditions. *J. Fluid Mech.* **841**, 1012–1039.

OBERLACK, M. 2001 A unified approach for symmetries in plane parallel turbulent shear flows. *J. Fluid Mech.* **427**, 299–328.

OBERLACK, M., CABOT, W., REIF, B.A.P. & WELLER, T. 2006 Group analysis, direct numerical simulation and modelling of a turbulent channel flow with streamwise rotation. *J. Fluid Mech.* **562**, 383–403.

PELZ, R.B., YAKHOT, V., ORSZAG, S.A., SHTILMAN, L. & LEVICH, E. 1985 Velocity-vorticity patterns in turbulent flow. *Phys. Rev. Lett.* **54** (23), 2505.

POLIFKE, W. & SHTILMAN, L. 1989 The dynamics of helical decaying turbulence. *Phys. Fluids* A*: Fluid Dyn.* **1** (12), 2025–2033.

POUQUET, A. & YOKOI, N. 2022 Helical fluid and MHD turbulence: a brief review. *Philos. Trans. R. Soc. A* **380** (2219), 20210087.

POVITSKY, A. 2017 Three-dimensional flow with elevated helicity in driven cavity by parallel walls moving in perpendicular directions. *Phys. Fluids* **29** (8), 083601.

SCHOPPA, W. & HUSSAIN, F. 2002 Coherent structure generation in near-wall turbulence. *J. Fluid Mech.* **453**, 57–108.

TEIMURAZOV, A.S., STEPANOV, R.A., VERMA, M.K., BARMAN, S., KUMAR, A. & SADHUKHAN, S. 2018 Direct numerical simulation of homogeneous isotropic helical turbulence with the TARANG code. *J. Appl. Mech. Tech. Phys.* **59** (7), 1279–1287.

TSINOBER, A. 2019 *Essence of Turbulence as a Physical Phenomenon*. Springer.

WALEFFE, F. 1992 The nature of triad interactions in homogeneous turbulence. *Phys. Fluids* A*: Fluid Dyn.* **4** (2), 350–363.

WALEFFE, F. 1993 Inertial transfers in the helical decomposition. *Phys. Fluids* A*: Fluid Dyn.* **5** (3), 677–685.

WANG, Y., HUANG, W. & XU, C. 2015 On hairpin vortex generation from near-wall streamwise vortices. *Acta Mechanica Sin.* **31** (2), 139–152.

WEISS, A., GARDNER, A.D., SCHWERMER, T., KLEIN, C. & RAFFEL, M. 2019 On the effect of rotational forces on rotor blade boundary-layer transition. *AIAA J.* **57** (1), 252–266.

XIA, Z., SHI, Y. & CHEN, S. 2016 Direct numerical simulation of turbulent channel flow with spanwise rotation. *J. Fluid Mech.* **788**, 42–56.

YAN, Z., LI, X. & YU, C. 2022 Helicity budget in turbulent channel flows with streamwise rotation. *Phys. Fluids* **34** (6), 065105.

YANG, Y.T., SU, W.D. & WU, J.Z. 2010 Helical-wave decomposition and applications to channel turbulence with streamwise rotation. *J. Fluid Mech.* **662**, 91–122.

YANG, Z., DENG, B.Q., WANG, B.C. & SHEN, L. 2018 Letter: the effects of streamwise system rotation on pressure fluctuations in a turbulent channel flow. *Phys. Fluids* **30** (9), 1–7.

YANG, Z., DENG, B.-Q., WANG, B.-C. & SHEN, L. 2020*a* On the self-constraint mechanism of the cross-stream secondary flow in a streamwise-rotating channel. *Phys. Fluids* **32** (10), 105115.

YANG, Z., DENG, B.-Q., WANG, B.-C. & SHEN, L. 2020*b* Sustaining mechanism of Taylor–Görtler-like vortices in a streamwise-rotating channel flow. *Phys. Rev. Fluids* **5** (4), 044601.

YANG, Z. & WANG, B.-C. 2018 Capturing Taylor–Görtler vortices in a streamwise-rotating channel at very high rotation numbers. *J. Fluid Mech.* **838**, 658–689.

YU, C., HU, R., YAN, Z. & LI, X. 2022 Helicity distributions and transfer in turbulent channel flows with streamwise rotation. *J. Fluid Mech.* **940**, A18.